

Feynman Diagrams for Matter Wave Interferometry

Jonah Glick* and Tim Kovachy

Department of Physics and Astronomy and Center for Fundamental Physics, Northwestern University

(Dated: July 17, 2024)

We introduce a new theoretical framework based on Feynman diagrams to compute phase shifts in matter wave interferometry. The method allows for analytic computation of higher order quantum corrections, beyond the traditional semi-classical approximation. These additional terms depend on the finite size of the initial matter wavefunction and/or have higher order dependence on \hbar . We apply the method to compute the response of matter wave interferometers to power law potentials and potentials with an arbitrary spatial dependence. The analytic expressions are validated by comparing to numerical simulations, and estimates are provided for the scale of the quantum corrections to the phase shift response to the gravitational field of the earth, anharmonic trapping potentials, and gravitational fields from local proof masses. We find that for certain experimentally feasible parameters, these corrections are large enough to be measured, and could lead to systematic errors if not accounted for. We anticipate these corrections will be especially important for trapped matter wave interferometers and for free-space matter wave interferometers in the presence of proof masses. These interferometers are becoming increasingly sensitive tools for mobile inertial sensing, gravity surveying, tests of gravity and its interplay with quantum mechanics, and searches for dark energy.

I. INTRODUCTION

Matter wave interferometry is a powerful tool for precision sensing and tests of fundamental physics. It is employed in a wide range of applications, including inertial navigation [1–4], gravity surveying [5–8], geodesy and geophysical studies [9, 10], tests of the equivalence principle and searches for fifth forces [11–24], measurements of Newton’s gravitational constant [25–27] and the fine structure constant [28, 29], searches for dark energy [30, 31], searches for dark matter [32–40], gravitational wave detection [8, 33, 34, 39–52], and tests of quantum mechanics and its interplay with gravity [53–64].

The calculation of the differential phase accumulated between two arms of a matter wave interferometer due to spatially varying external potentials has traditionally relied on a semi-classical approximation [9, 46, 65–70]. This approximation neglects the finite spatial extent of an individual arm of the matter wavefunction and excludes contributions to the phase shift at orders of \hbar higher than \hbar^{-1} [71]. While numerical simulation tools have been developed that do not rely on semi-classical approximations [72], analytical expressions have been highly valuable for understanding scalings of various contributions to the phase shift in order to guide experimental design and analysis [9, 66, 67].

We adapt the mathematical tools of quantum field theory (QFT) to introduce a Feynman diagram based approach to analytically computing the phase shift in a matter wave interferometer which incorporates higher-order quantum corrections from the finite extent of a matter wavefunction, and higher order terms in \hbar . Our approach is complementary to analyses based on Wigner function [73] or Magnus series [74] formalisms.

We find higher order quantum corrections to be especially relevant in trapped matter wave interferometers with small anharmonicities, where external potentials exhibit strong position dependence. This new diagrammatic tool can be used to generate analytic estimates of these corrections in interferometers confined to magnetic [75–79] and optical [80–89] potentials, which commonly consist of anharmonicities that can induce beyond-semi-classical phase shifts. Trapped interferometers are emerging as powerful tools for applications including mobile inertial sensing and gravity surveying [78, 80–86, 90], searches for dark energy and tests of gravity at short distances [87], and tests of quantum gravity [63]. Higher order quantum corrections will also be relevant to free-space interferometers that measure gravitational effects from local proof masses, like those aimed at obtaining precision measurements of Newton’s gravitational constant [25–27, 73] and testing the gravitational inverse square law to search for new fundamental interactions [11, 24]. As illustrative case studies, we identify examples in which these quantum corrections would yield a measurable effect in experimentally realistic trapped and proof-mass-style matter wave interferometers.

The paper is organized as follows: In Sec. II, we introduce the framework by reviewing the relevant background from QFT (Sec. II A), introducing one way to compute phase shifts in matter wave interferometry (Sec. II B), merge the two ideas to compute phase shifts with Feynman diagrams (Sec. II C), then make connections to the traditional semi-classical approach to computing phase shifts (Sec. II D). In Sec. III we apply the diagrammatic method to compute phase shifts under power law potentials. We investigate the validity of these expression by comparing to numerical evaluations of the phase shift in a certain parameter space, propagating wavepackets with the split step method [91]. We then take the analytic terms which emerge from the diagrammatic framework and use them to evaluate phase

* jonahglick2025@u.northwestern.edu

shifts from gravity gradients of the earth (Sec. III A), and for interferometers confined to anharmonic traps (Sec. III B). In Sec. IV, we sum over an infinite number of diagrams to produce an analytic expression for the phase shift response to an external potential with arbitrary spatial dependence, and apply the expression to estimate quantum corrections to the phase shift for a proof-mass style experiment.

II. FRAMEWORK FOR PHASE SHIFT CALCULATIONS

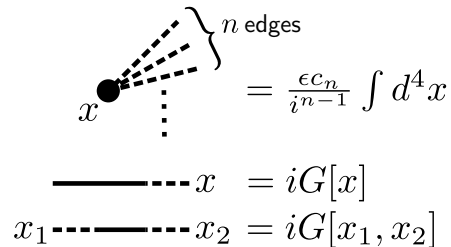
A. QFT Background

Here we express the key mathematical identity from QFT which we will apply to computing phase shifts in matter wave interferometry. Consider a scalar field theory with Lagrangian density $\mathcal{L} = \mathcal{L}_0 + \epsilon\mathcal{L}_1 + J\varphi$, where $\mathcal{L}_0 = -\frac{1}{2}\partial^\mu\varphi\partial_\mu\varphi - \frac{1}{2}m^2\varphi^2$ is the ‘free’ component of the Lagrangian density, \mathcal{L}_1 is a contribution that is third order or higher in φ , J is a source term, and ϵ is a perturbative parameter we can use to keep track of the orders of expansion. The ground state to ground state amplitude in this theory with a nonzero source term can be written as

$$\begin{aligned} \langle 0|0\rangle_J &= \int \mathcal{D}\varphi e^{i\int d^4x (\mathcal{L}_0 + \epsilon\mathcal{L}_1 + J\varphi)} \\ &= e^{i\int d^4x \epsilon\mathcal{L}_1 \left[\frac{1}{i}\frac{\delta}{\delta J(x)}\right]} \int \mathcal{D}\varphi e^{i\int d^4x (\mathcal{L}_0 + J\varphi)} \quad (1) \\ &= e^{i\int d^4x \epsilon\mathcal{L}_1 \left[\frac{1}{i}\frac{\delta}{\delta J(x)}\right]} e^{\frac{i}{2}\int d^4x_1 \int d^4x_2 J[x_1]G[x_1, x_2]J[x_2]} \end{aligned}$$

where for the second equality, we have made use of a well-established trick in QFT to take the nonlinear component of the Lagrangian density outside of the path integral by replacing its argument in φ with functional derivatives with respect to the source term J . The last equality highlights that after taking the nonlinear component of the Lagrangian density outside of the integrand, the path integral can be solved in closed form, where the *propagator* G is symmetric under an exchange of its arguments, $G[x_1, x_2] = G[x_2, x_1]$. [92–94]. For simplicity, we take $\hbar = 1$. One can solve for $\langle 0|0\rangle_J$ perturbatively in ϵ by Taylor expanding both exponentials in the last equality of Eq. 1 and applying the functional derivatives of the first exponential to the functionals of the second (see Appendix B). It is productive to organize the terms of this expansion with diagrams. The philosophy of Feynman diagrams is to ascribe value to the edges and vertices which compose a diagram so that a single diagram corresponds to a single term in the Taylor series expansion of Eq. 1. The four step process of diagrammatically computing the n^{th} order expansion of $\langle 0|0\rangle_J$ in ϵ is to 1. compute the value of the edges and vertices, 2. compose all n -vertex diagrams, 3. evaluate the integrals associated with the diagrams, and 4. sum the diagrams together. In the case

of perturbatively evaluating $\langle 0|0\rangle_J$ in ϵ , the value of the edges and vertices can be written as

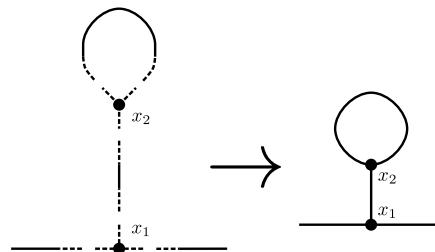


$$\begin{aligned} \text{Vertex } x \text{ with } n \text{ edges} &= \frac{\epsilon c_n}{i^{n-1}} \int d^4x \\ \text{Edge } x &= iG[x] \\ \text{Vertex } x_1 \text{---} x_2 &= iG[x_1, x_2] \end{aligned}$$

where $G[x] = \int d^4x' J[x']G[x', x]$, c_n is the n th order Taylor series coefficient in the expansion of \mathcal{L}_1 , $\mathcal{L}_1 = \sum_{i=0}^{\infty} \frac{1}{n!} c_n \varphi^n$, dashed lines correspond to connections of an edge and vertex (see example below), and x_i is the label of the vertex. The key identity we will be leveraging when we apply this formalism to phase shift calculations in matter wave interferometry is that the ground state to ground state amplitude can then be written as [92]

$$\langle 0|0\rangle_J = e^{\text{sum of all connected diagrams}} \quad (2)$$

where the value of each diagram is weighted by the inverse of the number of automorphisms of the diagram, also called the *symmetry factor*. As an example, consider an interaction $\mathcal{L}_1 = \frac{\epsilon_3}{3!} \varphi^3$. One of the diagrams which would contribute to the ϵ^2 order expansion of $\text{Log}[\langle 0|0\rangle_J]$ under this nonlinearity is



where according to the above values ascribed to the vertices and edges this diagram has value

$$\frac{1}{4} \left(\frac{\epsilon c_3}{i^{3-1}} \right)^2 \int d^4x_1 \int d^4x_2 (i)^4 G[x_1]^2 G[x_1, x_2] G[x_2, x_2]$$

and the factor of 1/4 comes from the inverse of the symmetry factor of the diagram. Further details can be found in [92–94].

B. Phase Shift Calculation Background

Here we will outline an approach to leveraging Eq. 2 to compute phase shifts in matter wave interferometry. Consider a system with one spatial dimension, x , and

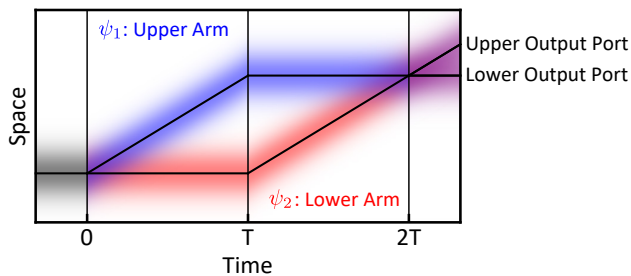


FIG. 1. A Mach-Zehnder interferometer sequence. Black solid lines denote classical trajectories, the blue corresponds to the wavepacket of the upper interferometer arm and the red corresponds to the lower interferometer arm. These arms are represented by wavefunctions ψ_1 and ψ_2 respectively. The gray density plot corresponds to the wavepacket before the first beamsplitter and the purple denote the interference of the blue and red interferometer arms. The vertical lines denote the times of the instantaneous beamsplitter and mirror operations.

one temporal dimension, t . The interferometer is composed of two arms which are represented by wavefunctions $\psi_1[x, t]$ and $\psi_2[x, t]$ respectively (see Fig. 1). We take these wavefunctions to arrive at the same output port of the interferometer. For simplicity, we assume the operations which split, re-direct, and interfere the two arms occur instantaneously. Take the first beamsplitter operation to be at time $t = 0$, and the time between laser pulses to be T in a Mach-Zehnder pulse sequence. Let us define t_i to be some *initial* time before the first beamsplitter operation $t_i < 0$, and t_f to be a *final* time after the second beamsplitter operation $t_f > 2T$. The interferometer contrast C and phase shift $\Delta\phi$ under spatial averaging can be expressed as

$$\frac{1}{2} \left(1 + C \cos[\Delta\phi] \right) = \frac{1}{4} \int_{-\infty}^{\infty} dx_f |\psi_1[x_f, t_f] + \psi_2[x_f, t_f]|^2$$

where we normalize the wavefunctions ψ_1 and ψ_2 so that the total probability associated with each is 1. The factor of $1/4$ comes from two factors of $1/\sqrt{2}$ from the first and final 50:50 beamsplitters, which are then squared under the modulus squared operation. Expanding out this equation, we have

$$\begin{aligned} & \frac{1}{4} + \frac{1}{4} + \frac{C}{4} e^{i\Delta\phi} + \frac{C}{4} e^{-i\Delta\phi} \\ &= \int_{-\infty}^{\infty} dx_b \left(\frac{1}{4} |\psi_1|^2 + \frac{1}{4} |\psi_2|^2 + \frac{1}{4} \psi_1 \psi_2^* + \frac{1}{4} \psi_1^* \psi_2 \right) \\ &= \frac{1}{4} + \frac{1}{4} + \int_{-\infty}^{\infty} dx_b \left(\frac{1}{4} \psi_1 \psi_2^* + \frac{1}{4} \psi_1^* \psi_2 \right) \end{aligned}$$

Then comparing cross terms in a manner consistent with the sign conventions of [66] results in

$$C e^{i\Delta\phi} = \int_{-\infty}^{\infty} dx_f \psi_1[x_f, t_f] \psi_2^*[x_f, t_f] \quad (3)$$

C. Computing Phase Shifts with Feynman Diagrams

We now derive an expression for the right hand side of Eq. 3 which will be structurally very similar to that of the last equality in Eq. 1 and which will enable us to diagrammatically compute phase shifts in matter wave interferometry. The amplitude associated with a trajectory which is located at position x_i at time t_i and located at position x_f at a later time t_f can be written following the Feynman path integral approach [95] as

$$K[x_f, t_f; x_i, t_i] = \int \mathcal{D}x[t] e^{\frac{i}{\hbar} S[\dot{x}, x, t]}$$

where S is the action associated with a classical path $x[t]$, and the path integral is performed over all paths which start at position x_i and time t_i and arrive at position x_f and time t_f . For the following sections of the paper, expressions will explicitly include dependence on \hbar . We can call this amplitude K the kernel propagator. Consider a system with Lagrangian $L = L_0[\dot{x}, x, t] + \epsilon L_1[x] + J[t]x$, where L_0 corresponds to the ‘free’ Lagrangian which consists of a kinetic energy term (with second order dependence on \dot{x}) and potential energy terms (containing only second order or lower dependence on x), L_1 consists of terms of any order in x , $J[t]$ is an external force, and ϵ is a perturbative parameter to keep track of the orders of expansion. This amplitude can be written as

$$\begin{aligned} & K[x_f, t_f; x_i, t_i; J[t]] \\ &= \int \mathcal{D}x[t] e^{\frac{i}{\hbar} \int_{t_i}^{t_f} dt (L_0 + \epsilon L_1[x] + J[t]x)} \\ &= e^{\frac{i}{\hbar} \int_{t_i}^{t_f} dt_1 \epsilon L_1 \left[\frac{\hbar}{i} \frac{\delta}{\delta J[t_1]} \right]} \int \mathcal{D}x[t] e^{\frac{i}{\hbar} \int_{t_i}^{t_f} dt (L_0 + J[t]x)} \quad (4) \\ &= e^{\frac{i}{\hbar} \int_{t_i}^{t_f} dt_1 \epsilon L_1 \left[\frac{\hbar}{i} \frac{\delta}{\delta J[t_1]} \right]} K^{(0)}[x_f, t_f; x_i, t_i; J[t]] \end{aligned}$$

where for notational convenience, the explicit dependence of x and \dot{x} on t , and the explicit dependence of L_0 on \dot{x} , x , and t is not written. We get the second equality by using the same integral trick used in Eq. 1, and we get the third equality by solving the path integral in closed form. We have explicitly written the dependence of the kernel propagator on the external force term $J[t]$. If the wave function of an matter wave at a time t_i just before the first beamsplitter of a Mach-Zehnder sequence is written as $\psi_0[x_i, t_i]$, then we can write the wave function that corresponds to the k^{th} arm of the interferometer, ψ_k , ($k = 1, 2$) as

$$\begin{aligned}
\psi_k[x_f, t_f] &= \int_{-\infty}^{\infty} dx_i K[x_f, t_f; x_i, t_i; J_k[t]] \psi_0[x_i, t_i] \\
&= e^{\frac{i}{\hbar} \int_{t_i}^{t_f} dt_1 \epsilon L_1 \left[\frac{\hbar}{i} \frac{\delta}{\delta J_k[t_1]} \right]} \\
&\quad \times \int_{-\infty}^{\infty} dx_i K^{(0)}[x_f, t_f; x_i, t_i; J_k[t]] \psi_0[x_i, t_i] \\
&= e^{\frac{i}{\hbar} \int_{t_i}^{t_f} dt_1 \epsilon L_1 \left[\frac{\hbar}{i} \frac{\delta}{\delta J_k[t_1]} \right]} \psi^{(0)}[x_f, t_f; J_k[t]]
\end{aligned} \tag{5}$$

where $\psi^{(0)}$ is a time evolved wavepacket in the unperturbed limit (under L_0 alone), and $J_k[t]$ is the effective force on by the k^{th} arm due to the recoil kicks of the matter wave interferometer. To get the first equality, we replaced K with its definition in Eq. 4 and took the functional derivative outside of the integral over x_i . In this work, we will take the initial wavefunction to have a Gaussian form, $\psi_0[x_i, t_i] = \left(\frac{2}{\pi w_0^2}\right)^{1/4} \exp\left[-\frac{1}{w_0^2} x_i^2\right]$, for which $\psi^{(0)}$ also has Gaussian form, since for Lagrangians L_0 with terms that are second order in \dot{x} and no more than second order in x , the kernel solution $K^{(0)}$ will have a Gaussian form [95], and an integral over a Gaussian is a Gaussian [96]. J_k can also have a time-independent component inducing a constant acceleration. Example forms for J , for a Mach-Zehnder interferometer sequence and a sequence where the two arms of the interferometer are kicked symmetrically, are given in in sections III A and III B respectively. Since the two arms are kicked differently, $J_1 \neq J_2$. We can now write Eq. 3 using Eq. 5 as

$$\begin{aligned}
C e^{i\Delta\phi} &= e^{\int_{t_i}^{t_f} dt_1 \epsilon \left(\frac{i}{\hbar} L_1 \left[\frac{\hbar}{i} \frac{\delta}{\delta J_1[t_1]} \right] + \frac{-i}{\hbar} L_1 \left[\frac{\hbar}{-i} \frac{\delta}{\delta J_2[t_1]} \right] \right)} \\
&\quad \times \int_{-\infty}^{\infty} dx_f \psi^{(0)}[x_f, t_f; J_1[t]] \psi^{(0)*}[x_f, t_f; J_2[t]] \\
&= e^{\int_{t_i}^{t_f} dt_1 \epsilon \left(\frac{i}{\hbar} L_1 \left[\frac{\hbar}{i} \frac{\delta}{\delta J_1[t_1]} \right] + \frac{-i}{\hbar} L_1 \left[\frac{\hbar}{-i} \frac{\delta}{\delta J_2[t_1]} \right] \right)} \\
&\quad \times \exp \left[\frac{1}{2} \int_{t_i}^{t_f} dt_1 \int_{t_i}^{t_f} dt_2 \left(J_1[t_1] G_{11}[t_1, t_2] J_1[t_2] \right. \right. \\
&\quad \quad \quad \left. \left. + J_1[t_1] G_{12}[t_1, t_2] J_2[t_2] \right. \right. \\
&\quad \quad \quad \left. \left. + J_2[t_2] G_{21}[t_1, t_2] J_1[t_2] \right. \right. \\
&\quad \quad \quad \left. \left. + J_2[t_2] G_{22}[t_1, t_2] J_2[t_2] \right) \right] \\
&= e^{\int_{t_i}^{t_f} dt_1 \epsilon \left(\frac{i}{\hbar} \delta_{a1} L_1 \left[\frac{\hbar}{i} \frac{\delta}{\delta J_a[t_1]} \right] + \frac{-i}{\hbar} \delta_{a2} L_1 \left[\frac{\hbar}{-i} \frac{\delta}{\delta J_a[t_1]} \right] \right)} \\
&\quad \times e^{\frac{1}{2} \int_{t_i}^{t_f} dt_1 \int_{t_i}^{t_f} dt_2 J_b[t_1] G_{bc}[t_1, t_2] J_c[t_2]}
\end{aligned} \tag{6}$$

where summation over repeated latin indices a, b, c is assumed, latin indices run from 1 to 2, and δ_{ij} is the Kronecker delta function. Details of this equality are worked

out in greater detail in Appendix A. Here the propagator G is symmetric about a swapping of the time variable arguments and latin indices together, $G_{ab}[t_1, t_2] = G_{ba}[t_2, t_1]$, which is a requirement for the Feynman diagram formalism to be applied. The exact form of $G_{ab}[t_1, t_2]$ for the case of a harmonic potential is worked out in Appendix A. In the unperturbed limit, the phase shift is calculated by evaluating just the right hand side of the last equality with $L_1 = 0$. Notice that the last equalities in Eq. 6 and Eq. 1 have similar forms, with the former including latin indices. It happens that despite the latin indices, we can ascribe value to diagrammatic components just as is done in QFT, such that

$$C e^{i\Delta\phi} = e^{\text{sum of all connected diagrams}} \tag{7}$$

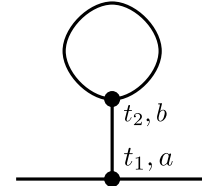
where components of the diagram have value

$$\begin{aligned}
&\text{Vertex with } n \text{ edges} = \lambda_a^n \int_{t_i}^{t_f} dt \\
&\text{Single edge } t, a = G_a[t] \\
&\text{Two-edge vertex } t_1, a \text{ --- } t_2, b = G_{ab}[t_1, t_2]
\end{aligned}$$

where $G_a[t] = \int_{t_i}^{t_f} dt' J_{a'}[t'] G_{a'a}[t', t_i]$, and

$$\lambda_a^n = \epsilon c_n \left(\left(\frac{\hbar}{i}\right)^{n-1} \delta_{a1} + \left(\frac{\hbar}{-i}\right)^{n-1} \delta_{a2} \right) \tag{8}$$

where the delta functions are Kronecker delta functions, and c_n is the n^{th} order Taylor series coefficient of $L_1[x]$. The focus of this paper will be on using Eq. 2 to solve Eq. 3 perturbatively in spatial potentials which render the equations of motion nonlinear. As an example, consider a system with a nonlinear potential $L_1 = \frac{c_3}{3!} x^3$. To compute a second order correction to the phase shift under this nonlinearity in the external potential, it will be productive to write down and sum all diagrams with two 3-point vertices. In parallel with the example in Sec. II A, one such diagram can be written as



where, following the rules above, the value of the diagram can be written as

$$\begin{aligned}
& \frac{1}{4} \lambda_a^3 \lambda_b^3 \int_{t_i}^{t_f} dt_1 \int_{t_i}^{t_f} dt_2 G_a[t_1]^2 G_{ab}[t_1, t_2] G_{bb}[t_2, t_2] \\
& = \frac{(\epsilon c_3)^2 \hbar^4}{4} \int_{t_i}^{t_f} dt_1 \int_{t_i}^{t_f} dt_2 \left(G_1[t_1]^2 G_{11}[t_1, t_2] G_{11}[t_2, t_2] \right. \\
& \quad + G_1[t_1]^2 G_{12}[t_1, t_2] G_{22}[t_2, t_2] \\
& \quad + G_2[t_1]^2 G_{21}[t_1, t_2] G_{11}[t_2, t_2] \\
& \quad \left. + G_2[t_1]^2 G_{22}[t_1, t_2] G_{22}[t_2, t_2] \right)
\end{aligned}$$

where we use Eq. 8 and sum over latin indices. Referencing Eq. 7, the contribution to the phase is then given by the imaginary part of this term, and the quantum corrections to the interferometer contrast are determined by taking the real part.

D. Connection to Traditional Semi-classical Framework

The traditional semi-classical approach to computing phase shifts involves separating the contributions of the phase into three parts : 1. a laser phase $\Delta\phi_{\text{laser}}$, which has to do with the imprint of the laser phase onto the matter waves, 2. a propagation phase $\Delta\phi_{\text{prop}}$, which has to do with the differential phase accumulated during the free propagation of the two arms under the spatially varying potential, and 3. a separation phase $\Delta\phi_{\text{sep}}$, which has to do with the two arms of the interferometer within the same output port not being perfectly overlapped with one another under spatial averaging. The total phase shift $\Delta\phi$ is expressed as a sum of these three components, $\Delta\phi = \Delta\phi_{\text{laser}} + \Delta\phi_{\text{prop}} + \Delta\phi_{\text{sep}}$ [9, 66].

In the diagram formalism, the propagation phase is associated with the convolution of wavepackets with kernels K , the separation phase is associated with the spatial averaging integrals over x_f in Eq. 6, and the laser phase is encoded in the external force term $J[t]$. In the semi-classical formalism, the laser phase associated with an individual interferometer arm can be written as $\sum_j \pm k_x x_{cl}[t_j]$ where the sum is over all kicks to the classical trajectory, $x_{cl}[t]$, indexed by j . Kick j occurs at time t_j , and k_x is the wavenumber of the light causing the kick. The sign of the phase imprint depends on the direction of the kick. In the limit of instantaneous matter-optics pulses, where $J[t]$ consists of delta functions in time (see for example Eq. 10 and Eq. 12), the laser kick can be thought of as applying an instantaneous phase shear across the wavepacket, akin to applying the operator $e^{\pm i \frac{m}{\hbar} v_r \hat{x}}$ to the wavepacket at the time of the pulse, where $v_r = \hbar k_x / m$ is the recoil velocity associated with the photon kick. The sign of the phase gradient depends on the direction of the kick. In the limit that the waist of the wavepacket is small relative to the phase gradient imprinted by the laser kick, this kick can be thought of as imprinting a phase $\pm k_x x_{cl}[t_j]$ onto the wavepacket, as in the semi-classical formalism.

There is a result in the semi-classical formalism that higher order quantum corrections do not contribute if the potential only has terms that are second order or lower in x [66]. For first order corrections from a perturbative potential, there is a way to see this in the diagram formalism. If there is no harmonic component included in L_0 , so that harmonic contributions to the Lagrangian are treated perturbatively, the one-vertex tree-level diagrams reproduce the semi-classical solution to first order in the perturbative potential. Higher-order quantum corrections for these one-vertex diagrams arise from loops (see Tab. I, where the leading order quantum correction comes from a diagram with a loop). Vertices and internal edges carry no dependence on $J[t]$, only external edges encode information about the laser kicks. ‘Bubble’ diagrams, which have no external edges, therefore carry no information about the interaction between the matter wave and the interferometer laser. If there is no interaction with the interferometer laser, there can be no phase shift, so these bubble diagrams always sum to zero. The fact that higher order than quadratic terms are required to induce beyond-semi-classical corrections to the phase shift arises in the diagram formalism by the fact that it is not possible to construct a diagram with one loop and at least one external edge using only a 2-point vertex. Only with a 3-point vertex (a cubic term in the Lagrangian) can a non-zero loop-level diagram be constructed, leading to higher order quantum corrections. In this context, an n -vertex diagram is a diagram with n vertices, and an n -point vertex is a vertex with n edges connected to it.

III. APPLICATION: COMPUTING PHASE SHIFTS FROM POWER LAW POTENTIALS

One can choose whether or not to include the harmonic component as part of the unperturbed component of the Lagrangian L_0 , or to include it as part of the perturbed component. In this section, we explore both options.

A. Treating Harmonic Terms Perturbatively

1. Diagram Values

In this section we use the rules outlined in Sec. IIB to evaluate the value of diagram elements for a free unperturbed potential, and use the diagrams to analytically compute phase shifts for matter wave interferometers subject to an external potential expressed as a power series in position. Consider a Lagrangian given in one spatial dimension z characterized by the Lagrangian $L = L_0[\dot{z}, z] + \epsilon L_1[z] + J[t]z$, where

$$\begin{aligned}
L_0 &= \frac{m}{2}\dot{z}^2 - mgz \\
L_1 &= -\left(\frac{m}{2}T_{zz}z^2 + \frac{m}{3!}Q_{zzz}z^3 + \frac{m}{4!}S_{zzzz}z^4 + \mathcal{O}[z^5]\right)
\end{aligned} \tag{9}$$

where T_{zz} , Q_{zzz} , and S_{zzzz} could correspond to terms in the Taylor series expansion in z of the Earth's gravitational field about the surface of the earth. With $L_1 = 0$, the interferometer phase can be computed by evaluating the spatial integrals of Sec II B, which results in

$$\begin{aligned}
G_{11}[t_j, t_k] &= \frac{1}{2m\hbar} \left(-\beta t_j t_k - \frac{1}{\beta} + i|t_j - t_k| \right) \\
G_{12}[t_j, t_k] &= \frac{1}{2m\hbar} \left(\beta t_j t_k + \frac{1}{\beta} + i(t_j - t_k) \right) \\
G_{21}[t_j, t_k] &= \frac{1}{2m\hbar} \left(\beta t_j t_k + \frac{1}{\beta} - i(t_j - t_k) \right) \\
G_{22}[t_j, t_k] &= \frac{1}{2m\hbar} \left(-\beta t_j t_k - \frac{1}{\beta} - i|t_j - t_k| \right)
\end{aligned}$$

where $\beta = 2\hbar/mw_0^2$. This calculation is done in detail in Appendix A. For a Mach-Zhender interferometer, the external force term has the form

$$\frac{J_a[t]}{m} = -g + \begin{cases} v_r \delta[t - 0] - v_r \delta[t - T], & a = 1 \\ v_r \delta[t - T] - v_r \delta[t - 2T], & a = 2 \end{cases} \tag{10}$$

corresponding to interference between the two arms in the the 'lower' output port of the interferometer referencing Fig. 1. J_1 corresponds to the kicks on the 'upper' arm of the interferometer, and J_2 corresponds to the kicks on the 'lower' arm. Alternate pulse sequences can be computed by adding/modifying terms that are proportional to the recoil velocity v_r . In this system, the value of the external vertices can be expressed in terms of the semi-classical trajectories of the interferometer arms

$$\begin{aligned}
G_1[t] &= \frac{i}{\hbar} z_{\text{cl},1}^{(0)}[t] \\
G_2[t] &= -\frac{i}{\hbar} z_{\text{cl},2}^{(0)}[t]
\end{aligned} \tag{11}$$

where $z_{\text{cl},1}^{(0)}[t]$ and $z_{\text{cl},2}^{(0)}[t]$ are the unperturbed classical trajectories of the two interferometer arms, which evolve under the Lagrangian L_0 . Eq. 11 holds even when we account for a nonzero initial position z_0 and velocity v_z of the classical trajectory. See Appendix A for more details. We now use these rules to compute phase shifts under power law potentials.

2. Validating with Numerics

Here we demonstrate agreement between the diagrammatic approach to computing phase shifts and an ab-

initio numerical evaluation of the phase shift which accounts for the contributions that emerge from the finite-size nature of the matter wavepacket. Consider the Lagrangian of Eq. 9 with $T_{zz} = S_{zzzz} = 0$ and no higher order terms in z . We leverage the split-step [91] approach to numerically time evolve matter wavepackets in this power-law potential. We independently time evolve the two wavepackets associated with the two interferometer arms. The instantaneous laser kicks are performed by applying linear phase gradients across the two wavefunctions between discrete time steps. The phase is then extracted by performing a discrete sum over spatial coordinates to evaluate $P_{\text{lower}}[\phi_b]$, the population in the 'lower' output port, for different values of the final beamsplitter phase ϕ_b , $P_{\text{lower}}[\phi] = \int_{-\infty}^{\infty} dz_f |\psi_1[z_f, t_f] + \psi_2[z_f, t_f] e^{-i\phi_b}|^2$ for 63 evenly spaced values of ϕ between 0 and 2π at the time immediately following the final beamsplitter, then fitting P_{lower} to the function $\frac{1}{2}(1 + C \cos[\Delta\phi + \phi_b])$ with fit parameters C , the interferometer contrast, and $\Delta\phi$, the interferometer phase shift. Here ψ_1 is the wavefunction which corresponds to the 'upper' interferometer arm in Fig. 1.

We run these simulations to verify the mathematical approach, and use unphysical parameters (e.g. larger values of \hbar) to amplify quantum corrections and reduce computational complexity. Realistic physical parameters require high spatial-temporal resolution for accuracy, which increases computation time. These simulations do not represent expected phase shifts, but serve to validate the analytic terms which come out of the diagrammatic formalism. The analytic terms are then used to estimate realistic phase shifts (see Sections III A 3, III B 3, and IV C). Figure 2 plots the interferometer phase shift as a function of interrogation time under this power-law potential computed in three different ways: 1. numerically (black dots), 2. via the traditional semi-classical approach (dashed gray line), and 3. via the diagrammatic approach (solid gray line). In both the semi-classical and diagrammatic approaches, we compute only the first order contribution in Q_{zzz} . The two contributing diagrams are indicated in panel (a). Simulation parameters are indicated in the caption. In this parameter space, the terms that emerge from the diagrammatic calculator have strong agreement with the output of the split-step numerics, whereas the semi-classical approach deviates more strongly from the numerical results. Panel (b) of Fig. 2 displays the classical trajectories of the two interferometer arms (black lines) for a $T = 100$ ms interferometer sequence. The gray density plot indicates the wavepacket waist before the first beamsplitter operation at time $t = 0$. The blue density plot indicates the wavepacket associated with the 'upper' interferometer arm, and the red wavepacket corresponds to the 'lower' interferometer arm. The diagrammatic approach re-produces the terms which emerge from the semi-classical solver, and produce new terms associated with higher order quantum corrections. Let us define the interferometer phase shift $\Delta\phi$ as a sum of the semi-

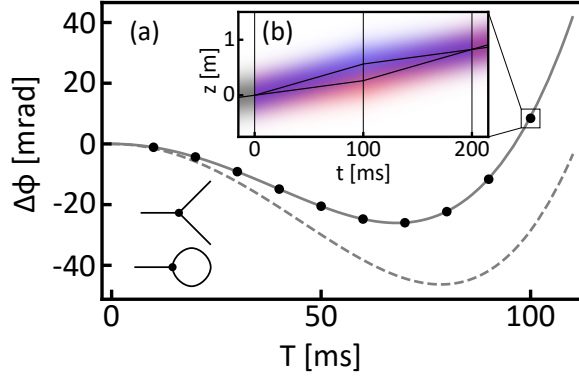


FIG. 2. (a) Phase shifts under the Lagrangian $L = m\dot{z}^2/2 - mgz - mQ_{zzz}z^3/3!$ as computed numerically (black dots), via the traditional semi-classical formalism (gray dashed line), and computed diagrammatically (gray solid line). The diagrams which contribute to the leading order correction in Q_{zzz} are indicated in the bottom left hand side. The simulation parameters are as follows, with each parameter expressed in SI units: $\hbar/m = 10^{-2}$, $w_0 = 0.5$, $v_r = 3$, $v_z = 2.63$, $z_0 = 0$, $g = 0.05$, $Q_{zzz} = -0.4$, $T_{zz} = S_{zzzz} = 0$, and no higher order potential terms. The split step numerics were done with spatial resolution $\Delta z = 2.5$ mm, a temporal resolution of $\Delta t = 0.5$ ms, and a grid centered at $z = 0$ with a size of 4 m. (b) The span of the two interferometer arms for $T = 100$ ms. The gray density plot indicates the width of the wavefunction before the first beamsplitter. The first beamsplitter operation splits the wavefunction into an upper arm (blue) and lower arm (red). The final beamsplitter then interferes the two arms (purple). The classical trajectories are indicated with solid black lines.

classically accumulated phase and quantum corrections, $\Delta\phi = \Delta\phi_{\text{cl}} + \Delta\phi_{\text{qu}}$. The terms which emerge from the diagrammatic calculation but which do not emerge from the semi-classical calculation to first order in Q_{zzz} are $\Delta\phi_{\text{qu}} = -Q_{zzz}(\frac{1}{4\beta}v_r T^2 + \frac{7}{24}\beta v_r T^4) + \mathcal{O}[Q_{zzz}^2]$. These quantum correction terms are the source of the disagreement between the semi-classically calculated phase shift and the diagrammatically calculated phase shift in Fig. 2.

3. Calculation of Higher Order Quantum Corrections under Gravity Gradients of the Earth

To explore the extent to which these higher order quantum corrections under power law potentials associated with the spherical nature of the Earth could be measured with a state-of-the-art matter wave interferometer, we take the analytic expressions that come out of the diagrammatic formalism, and plug in typical operating parameters (parameters indicated in the caption of Table I). In Table I, we rank each of the terms that come out of this calculation in order of the size of their contribution to the interferometer phase shift, with the higher order quantum correction terms highlighted gray. The largest term that cannot be captured by the semi-

TABLE I. Phase shift terms for a 1D Mach-Zehnder matter wave interferometer subject to gravity gradients associated with the spherical nature of the Earth, along with the diagrams which produce the term, ranked in order of the magnitude of their contribution to the total phase shift. The phase shifts are computed with the following parameters: $w_0 = 1$ mm, $k_z = 2\pi/(698$ nm), $v_z = 3$ m/s, $T = 1$ s, $g = 9.8$ m/s², $T_{zz} = -2g/R$, $Q_{zzz} = 6g/R^2$, $S_{zzzz} = -24g/R^3$, $z_0 = 0$, $R = 6.38 \times 10^6$ m, $m = 86.91u$, $\beta = 2\hbar/(mw_0^2)$. The largest quantum correction term is highlighted in light gray.

	Phase Shift	Size [rad]	Diagram
1	$-\frac{m}{\hbar} g v_r T^2$	-8.82×10^7	
2	$\frac{7}{12} \frac{m}{\hbar} g v_r T^4 T_{zz}$	-1.58×10^2	
3	$-\frac{m}{\hbar} v_r v_z T^3 T_{zz}$	8.30×10^1	
4	$-\frac{1}{2} \frac{m}{\hbar} v_r^2 T^3 T_{zz}$	9.10×10^{-2}	
5	$-\frac{31}{120} \frac{m}{\hbar} g^2 v_r T^6 Q_{zzz}$	-3.23×10^{-4}	
6	$\frac{3}{4} \frac{m}{\hbar} g v_r v_z T^5 Q_{zzz}$	2.87×10^{-4}	
7	$-\frac{31}{360} \frac{m}{\hbar} g v_r T^6 T_{zz}^2$	-7.17×10^{-5}	
8	$-\frac{7}{12} \frac{m}{\hbar} v_r v_z^2 T^4 Q_{zzz}$	-6.83×10^{-5}	
9	$\frac{1}{4} \frac{m}{\hbar} v_r v_z T^5 T_{zz}^2$	6.38×10^{-5}	
10	$\frac{3}{8} \frac{m}{\hbar} g v_r^2 T^5 Q_{zzz}$	3.14×10^{-7}	
11	$-\frac{7}{12} \frac{m}{\hbar} v_r^2 v_z T^4 Q_{zzz}$	-1.50×10^{-7}	
12	$\frac{1}{8} \frac{m}{\hbar} v_r^2 T^5 T_{zz}^2$	6.99×10^{-8}	
13	$-\frac{3}{8} \frac{m}{\hbar} g^2 v_r v_z T^7 S_{zzzz}$	8.81×10^{-10}	
14	$\frac{127}{1344} \frac{m}{\hbar} g^3 v_r T^8 S_{zzzz}$	-7.25×10^{-10}	
15	$-\frac{9}{20} \frac{m}{\hbar} g v_r v_z T^7 Q_{zzz} T_{zz}$	5.29×10^{-10}	
16	$\frac{127}{1120} \frac{m}{\hbar} g^2 v_r T^8 Q_{zzz} T_{zz}$	-4.35×10^{-10}	
17	$\frac{31}{60} \frac{m}{\hbar} g v_r v_z^2 T^6 S_{zzzz}$	-3.72×10^{-10}	
18	$\frac{31}{72} \frac{m}{\hbar} v_r v_z^2 T^6 Q_{zzz} T_{zz}$	-1.55×10^{-10}	
19	$-\frac{1}{6} \frac{m}{\hbar} v_r^3 T^4 Q_{zzz}$	-9.38×10^{-11}	
20	$-\frac{1}{4} \frac{m}{\hbar} v_r v_z^3 T^5 S_{zzzz}$	5.50×10^{-11}	
21	$-\frac{1}{40} \frac{m}{\hbar} v_r v_z T^7 T_{zz}^3$	1.96×10^{-11}	
22	$\frac{127}{20160} \frac{m}{\hbar} g v_r T^8 T_{zz}^3$	-1.61×10^{-11}	
23	$-\frac{1}{4} \frac{1}{\beta} v_r T^2 Q_{zzz}$	-1.63×10^{-12}	
24	$-\frac{3}{16} \frac{m}{\hbar} g^2 v_r^2 T^7 S_{zzzz}$	9.66×10^{-13}	
25	$\frac{31}{60} \frac{m}{\hbar} g v_r v_z T^6 S_{zzzz}$	-8.15×10^{-13}	

classical formalism comes in with a relative scaling of one part in 10^{20} with respect to the largest overall $-kgT^2$ term. This higher order quantum contribution to the phase shift is generally below the sensitivity of modern day matter wave interferometers. Quantum corrections to phase shifts coming from gravity gradients associated with the spherical nature of the Earth might not to be seen in the near future.

B. Including a Harmonic Component as Part of the Unperturbed Lagrangian

1. Diagram Values

In previous sections we considered treating the harmonic component of the potential (with strength T_{zz}) perturbatively. Consider now a Lagrangian describing a matter wave confined inside of an anharmonic potential with harmonic component $\omega = \sqrt{T_{zz}}$, and a small cubic component Q_{zzz} , so that the Lagrangian can be described by

$$L_0 = \frac{m}{2}\dot{z}^2 - \frac{1}{2}m\omega^2 z^2$$

$$L_1 = -mQ_{zzz}z^3$$

In the case that we absorb the harmonic component of the potential as part of the unperturbed solution, the value of the internal edges of the diagram can be expressed as

$$G_{11}[t_j, t_k] = \frac{1}{2m\hbar} \left(-\frac{\beta \sin[\omega t_j] \sin[\omega t_k]}{\omega^2} - \frac{\cos[\omega t_j] \cos[\omega t_k]}{\beta} + i \frac{\sin[\omega |t_j - t_k|]}{\omega} \right)$$

$$G_{12}[t_j, t_k] = \frac{1}{2m\hbar} \left(\frac{\beta \sin[\omega t_j] \sin[\omega t_k]}{\omega^2} + \frac{\cos[\omega t_j] \cos[\omega t_k]}{\beta} + i \frac{\sin[\omega (t_j - t_k)]}{\omega} \right)$$

$$G_{21}[t_j, t_k] = \frac{1}{2m\hbar} \left(\frac{\beta \sin[\omega t_j] \sin[\omega t_k]}{\omega^2} + \frac{\cos[\omega t_j] \cos[\omega t_k]}{\beta} - i \frac{\sin[\omega (t_j - t_k)]}{\omega} \right)$$

$$G_{22}[t_j, t_k] = \frac{1}{2m\hbar} \left(-\frac{\beta \sin[\omega t_j] \sin[\omega t_k]}{\omega^2} - \frac{\cos[\omega t_j] \cos[\omega t_k]}{\beta} - i \frac{\sin[\omega |t_j - t_k|]}{\omega} \right)$$

Details of this calculation can be found in Appendix A. Note that this value for propagators G_{ab} asymptote as $\omega \rightarrow 0$ to the propagator value of Sec. III A, where we did not include a harmonic component of the potential in L_0 . The value of the vertex is the same as in Eq. 8 and the value of the external edges $G_a[t]$ is as it is defined in Sec. IIB, which in this case has a more complicated form than just being proportional to the unperturbed classical trajectory of the arm. Its form depends on the form of the kicks J , and its value is explicitly written out in Appendix A. Consider an interferometer sequence where the two arms are kicked symmetrically, and the external force on the two arms which emerge in the same output port is expressed by

$$\frac{J_a[t]}{mv_r} = \begin{cases} 2\delta[t-0] - 4\delta[t-T] + 2\delta[t-2T] & a=1 \\ -2\delta[t-0] + 4\delta[t-T] - 2\delta[t-2T] & a=2 \end{cases} \quad (12)$$

Here one arm of the interferometer ($a=1$) is kicked with 2 recoils ‘upward’ at time $t=0$, 4 recoils ‘downward’ at time $t=T$, and 2 recoils ‘upward’ at time $t=2T$. The other arm ($a=2$) is kicked with equal and opposite recoils to the first. We take the initial center-of-mass (COM) position and velocity of the Gaussian wavepacket to be zero. In this case, under only a harmonic potential, the phase shift would be zero owing to the mirror symmetry of the potential and the symmetry with which the two arms of the interferometer are kicked. The small cubic non-linearity in L_1 breaks that mirror symmetry and produces a non zero phase shift.

There is a way in which the semi-classical approach to computing phase shifts breaks down. It is the case that the phase shift of an interferometer does not change after the final beamsplitter. In the semi-classical formalism, and in the absence of a cubic nonlinearity, this property is satisfied by the fact that the additional accumulated separation phase between two the arms which compose a single output port exactly cancels with the additionally accumulated propagation phase after the final beamsplitter. Under a cubic nonlinearity, however, the propagation and separation phases accumulated after the final beamsplitter no longer cancel, and what results is a computed phase shift which changes as a function of the time after the final beamsplitter. In the diagrammatic approach, on the other hand, the phase shift is correctly predicted to be independent of the time after the final beamsplitter pulse.

2. Validating with Numerics

To demonstrate agreement with evaluating the phase shift numerically, as in Sec. III A 2, we evaluate phase shifts in a parameter space where quantum corrections are heightened beyond physical realism (parameters indicated in caption of Fig. 3). Fig. 3 compares the result of evaluating these phase shifts numerically (black dots), via the semi-classical formalism (dashed gray line), and via the diagrammatic formalism (solid gray line). The semi-classical solution is plotted evaluating the phase shift at the time immediately following the final beamsplitter, even though technically its value changes as a function of time after the final beamsplitter as discussed earlier. The two three-vertex diagrams which contribute to the phase shift are included in an inset of panel (a). Panel (b) indicates the semi classical trajectories of the two interferometer arms (black lines), along with the wavepacket size (blue for the upper arm and red for the lower). Panel (c) plots the shape of the potential, which is anharmonic owing to a small cubic dependence which breaks the mirror symmetry of the system about $z=0$.

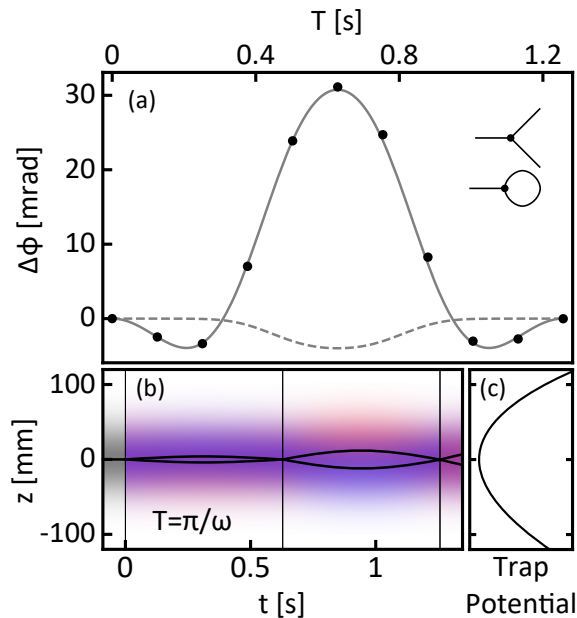


FIG. 3. Simulation of matter wave interferometer confined to an anharmonic trap. Simulation parameters (in SI units) are $\hbar/m = 10^{-2}$, $w_0 = 0.0632456$, $\omega = 5$, $v_z = 0$, $v_r = 10^{-2}$, $Q_{zzz} = 10^2$, $\Delta z = 5 \times 10^{-4}$, $\Delta t = 5 \times 10^{-4}$. The waist w_0 is chosen so that the initial wavepacket is the ground state of the harmonic potential. (a) Numerically computed phase shifts (black dots), along with the semi-classically computed phase (dashed gray line) and diagrammatically computed phase (solid gray line). The two diagrams that contribute to the leading order phase shift in Q_{zzz} are displayed on the right hand side. (b) Classical trajectories of the two interferometer arms (solid black lines) along with the width of the wavepackets associated with both interferometer arms (blue and red). The trajectories are plotted for the interrogation time for which the phase shift is maximized ($T = \pi/\omega$). (c) The form of the anharmonic trapping potential, to contextualize the classical trajectories.

3. Calculating Phase Shifts in Matter Wave Interferometers Confined in Anharmonic Traps

Here we apply the analytic expressions which emerge from the diagrammatic formalism to an experimentally realistic case of a matter wave confined to a magnetic trap [97]. Following the experimental parameters of a time-orbiting potential magnetic trap used for Bose-Einstein condensate atom interferometry [98], we consider a trap frequency of $\omega = 2\pi \times 11.2$ Hz, a trap anharmonicity of $Q_{zzz} = 9.98 \times 10^6 \text{m}^{-2}\text{s}^{-1}$, no initial COM velocity, a recoil velocity of $v_r \approx 5.89$ mm/s, and an initial wavepacket waist of $w_0 = 10 \mu\text{m}$ [99]. The value of w_0 comes from the observed condensate size in [100]. Figure 4 shows expected phase shifts under a sequence where the two arms are kicked symmetrically. In this scenario, the quantum corrections are on the order of the semi-classically computed phase shifts. The leading-order quantum corrections are approximately 1 mrad and might therefore

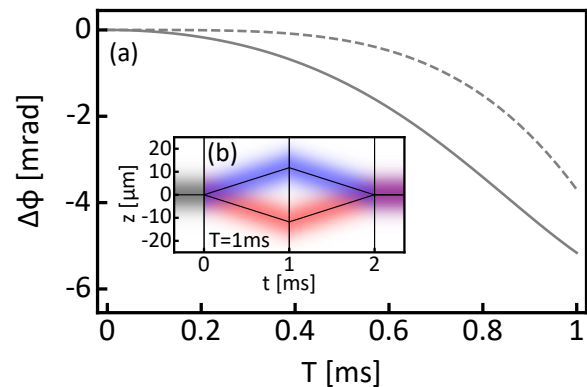


FIG. 4. (a) Quantum corrections for a trapped matter wave interferometer with experimentally realistic parameters, computed via the semi-classical method (dashed gray line) and the diagrammatic method (solid gray line). In the semi-classical computation, the phase shift is evaluated immediately after the final beamsplitter. (b) The corresponding interferometer arms for a 1 ms interrogation time interferometer sequence. The black lines indicate the classical trajectories and the blue and red density plots indicate the wavepacket waist of the two interferometer arms. The computed interferometer contrast drops to $\approx 73\%$ at $T = 1$ ms owing to the two arms of the interferometer imperfectly overlapping at the time of the final beamsplitter.

be observable. This example suggests that beyond-semiclassical corrections to the interferometer phase could be important to consider for accurately modeling trapped interferometers.

IV. APPLICATION: PHASE SHIFT FOR POTENTIALS WITH ARBITRARY SPATIAL DEPENDENCE

In this section, we will consider external potential with more complicated dependence on z . We will use the diagrammatic formalism outlined in Sec. II B to compute phase shifts to all orders in z , but only first order in ϵ by summing over all 1-vertex diagrams.

A. Calculation of Phase Shift by Summing Over All 1-Vertex Diagrams

Consider the Lagrangian

$$L_1 = -m\phi_g[z]$$

where ϕ_g is a gravitational potential with an arbitrary spatial dependence. We will write out the value of a diagram with an arbitrary number of external edges and loops, then sum over the number of external edges and loops. This will amount to summing over the potentially infinite number of one vertex diagrams associated

with the potentially infinite number of Taylor series coefficients in the potential $\phi_g[z] = \sum_{n=0}^{\infty} \frac{1}{n!} c_n z^n$. A diagram with j external edges and k loops will have value $\mathcal{A}[j, k]$, where

$$\mathcal{A}[j, k] =$$

We can write the value of this diagram in terms of the symmetry factor, vertex value, and edge values as $\mathcal{A}[j, k] = (SYM)(VERT)(EDGE)$ with

$$\begin{aligned} SYM &= \frac{1}{j!k!2^k} \\ VERT &= (-m)\lambda_a^{j+2k} \int_{t_i}^{t_f} dt \\ EDGE &= (G_a[t])^j (G_{aa}[t, t])^k \end{aligned}$$

Using Eq. 8, we can write this value as $\mathcal{A}[j, k] = \mathcal{A}_1[j, k] + \mathcal{A}_2[j, k]$ where we can write

$$\lambda_a^{j+2k} = \sum_{\alpha=1}^2 \left((-1)^{\alpha+1} \frac{\hbar}{i} \right)^{j+2k-1} (-m\epsilon) c_{j+2k} \delta_{a\alpha}$$

$$\begin{aligned} \mathcal{A}_\alpha[j, k] &= \frac{1}{j!k!2^k} \left((-1)^{\alpha+1} \frac{\hbar}{i} \right)^{j+2k-1} (-m\epsilon) c_{j+2k} \\ &\times \int_{t_i}^{t_f} dt (G_\alpha[t])^j (G_{\alpha\alpha}[t, t])^k \end{aligned} \quad (13)$$

with $\alpha = 1, 2$. To arrive at this equality, we apply the Kronecker delta function inside of λ_a^{j+2k} to the edge values in the integrand. We can solve for the phase shift by summing over the number of external edges and loops. If we express the phase shift as a Taylor series in ϵ , $\Delta\phi = \Delta\phi^{(0)} + \Delta\phi^{(1)}\epsilon + \mathcal{O}[\epsilon^2]$, then

$$\Delta\phi^{(1)} = \text{Im} \left[\sum_{\alpha=1}^2 \sum_{j=0}^{\infty} \sum_{k=0}^{\infty} \mathcal{A}_\alpha[j, k] \right]$$

We start by evaluating the sum over the number of external edges j

$$\begin{aligned} \sum_{j=0}^{\infty} \mathcal{A}_\alpha[j, k] &= -m\epsilon \int_{t_i}^{t_f} dt \frac{1}{k!2^k} \left((-1)^{\alpha+1} \frac{\hbar}{i} \right)^{2k-1} (G_{\alpha\alpha}[t, t])^k \\ &\times \sum_{j=0}^{\infty} \frac{1}{j!} c_{j+2k} \left((-1)^{\alpha+1} \frac{\hbar}{i} G_\alpha[t] \right)^j \\ &= -m\epsilon \int_{t_i}^{t_f} dt \frac{1}{k!2^k} \left((-1)^{\alpha+1} \frac{\hbar}{i} \right)^{2k-1} (G_{\alpha\alpha}[t, t])^k \\ &\times \partial_z^{2k} \phi_g[z] \Big|_{z=(-1)^{\alpha+1} \frac{\hbar}{i} G_\alpha[t]} \end{aligned} \quad (14)$$

where to arrive at the second equality, we applied the identity $\sum_{j=0}^{\infty} \frac{1}{j!} c_{j+2k} z^j = \partial_z^{2k} \sum_{j=0}^{\infty} \frac{1}{j!} c_j z^j = \partial_z^{2k} \phi_g[z]$. Now performing the sum over the number of loops k , we have

$$\begin{aligned} &\sum_{k=0}^{\infty} \sum_{j=0}^{\infty} \mathcal{A}_\alpha[j, k] \\ &= -m\epsilon \left((-1)^{\alpha+1} \frac{\hbar}{i} \right)^{-1} \int_{t_i}^{t_f} dt \\ &\times \sum_{k=0}^{\infty} \frac{1}{k!} \left(-\frac{1}{2} \hbar^2 G_{\alpha\alpha}[t, t] \partial_z^2 \right)^k \phi_g[z] \Big|_{z=(-1)^{\alpha+1} \frac{\hbar}{i} G_\alpha[t]} \\ &= -m\epsilon (-1)^{\alpha+1} \frac{i}{\hbar} \int_{t_i}^{t_f} dt \\ &\times e^{-\frac{1}{2} \hbar^2 G_{\alpha\alpha}[t, t] \partial_z^2} \phi_g[z] \Big|_{z=(-1)^{\alpha+1} \frac{\hbar}{i} G_\alpha[t]} \\ &= (-1)^{\alpha+1} \frac{-im\epsilon}{\hbar} \int_{t_i}^{t_f} dt \bar{\phi}_g \left[i\hbar (-1)^\alpha G_\alpha[t], t \right] \end{aligned}$$

with

$$\begin{aligned} \bar{\phi}_g[z, t] &= \int_{-\infty}^{\infty} dz' \left(\frac{1}{-2\pi\hbar^2 G_{\alpha\alpha}[t, t]} \right)^{1/2} \\ &\times e^{\frac{1}{2\hbar^2 G_{\alpha\alpha}[t, t]} (z-z')^2} \phi_g[z'] \end{aligned}$$

where to arrive at the third equality, we used the identity [101]

$$e^{a\partial_x^2} \phi_g[x] = \int_{-\infty}^{\infty} dx' \left(\frac{1}{4\pi a} \right)^{1/2} e^{-\frac{1}{4a}(x-x')^2} \phi_g[x']$$

This expression is valid whether we include a harmonic component as part of the unperturbed potential or not. If we choose not to include a harmonic component as part of the unperturbed potential, such that

$$L_0 = \frac{m}{2} \dot{z}^2 - mgz$$

then referencing the propagators of Sec. III A, we have

$$G_{11}[t, t] = G_{22}[t, t] = -\frac{1}{2m\hbar} \left(\beta t^2 + \frac{1}{\beta} \right)$$

and referencing the external edge values of Eq. 11, the first order correction to the phase shift can be written out as

$$\Delta\phi^{(1)} = -\frac{m}{\hbar} \int_{t_i}^{t_f} dt \left(\bar{\phi}_g[z_{\text{cl},1}^{(0)}[t], t] - \bar{\phi}_g[z_{\text{cl},2}^{(0)}[t], t] \right) \quad (15)$$

where

$$\bar{\phi}_g[z, t] = \int_{-\infty}^{\infty} dz' \left(\frac{1}{\pi(\hbar/m)(\beta t^2 + 1/\beta)} \right)^{1/2} \times e^{-\frac{1}{(\hbar/m)(\beta t^2 + 1/\beta)}(z-z')^2} \phi_g[z']$$

Each one-vertex diagram has pure imaginary value, resulting in no corrections to the contrast at first order in the potential ϕ_g . For comparison, following the usual semi-classical formalism, the correction to the phase shift to first order in the potential can be written as [65]

$$\Delta\phi^{(1)} = -\frac{m}{\hbar} \int_{t_i}^{t_f} dt \left(\phi_g[z_{\text{cl},1}^{(0)}[t]] - \phi_g[z_{\text{cl},2}^{(0)}[t]] \right) \quad (16)$$

if the unperturbed classical trajectories have the same position and velocity at the time of the final beamsplitter. We now use Eq. 15 to compute higher order quantum corrections to matter wave interferometers under more interesting spatial dependent potentials.

B. Agreement With Numerics

Here we validate Eq. 15 by numerically solving for the phase response of a matter wave interferometer to the gravitational potential from a proof mass. We use nonphysical simulation parameters to amplify quantum corrections, as done in Sections III A 2, and III B 2. In Sec. IV C, we estimate the phase response using realistic experimental parameters.

Consider a system where the gravitational potential $\phi_g[z]$ emerges from a 1D ring shaped proof mass with radius R and total mass M aligned with the interferometer axis z , along with a linear gravity term from the Earth, such that the potential contributed by the proof mass has the form

$$\phi_g[z] = -\frac{GM}{\sqrt{R^2 + z^2}} \quad (17)$$

where G is Newton's gravitational constant, and the unperturbed Lagrangian does not have the harmonic component included, $L_0 = m\dot{z}^2/2 - mgz$. This potential has an infinite number of Taylor series coefficients in z , so computing phase shifts perturbatively in z could lead to inaccurate predictions. In Fig. 5, we display the result of computing the phase shift in an unphysical parameter space where quantum corrections are heightened (see

caption for simulation parameters). Panel (a) contains the phase shift as determined by a split step wavepacket simulation (black dots), the semi-classical method (gray dashed line) and the diagrammatic method (gray solid line). The semi-classical phase shift is determined by numerically evaluating the integral over time of Eq. 16, and the diagrammatic phase shift calculation is performed by numerically evaluating the integrals over space and time of Eq. 15. The inset of that panel indicates the summation that is performed to arrive at the diagrammatically evaluated phase shift. Here we plot the first order correction in ϵ , which in this case is also the first order correction in Newton's gravitational constant G . $\Delta\phi = \Delta\phi^{(0)} + \Delta\phi^{(1)}G + \mathcal{O}[G^2]$, where $\Delta\phi^{(0)} = -\frac{m}{\hbar}v_r g T^2$. The Mach-Zehnder pulse sequence simulated here corresponds to a source term J_a that has the same form as that of Eq. 10.

The 'smearing' effect on the phase response of the interferometer, resulting from incorporating the finite size of the matter wavepacket into the phase shift calculation, suppresses the peak response from the semi-classically computed phase. This suppression highlights how higher order quantum corrections could manifest as sources of systematic error. Panel (b) presents the semi-classical trajectories (black lines) associated with the two interferometer arms in this parameter space for $T = 0.5$ s. The density plot indicates the finite extent of the wavepackets of the two interferometer arms (blue and red). Panel (c) shows the shape of the external potential $\phi_g[z]$ in relation to the classical trajectories and the size of the wavepackets.

C. Calculating Response of Matter Wave Interferometer to Proof-Mass Potential

Here we use Eq. 15 to estimate the scale of quantum corrections under realistic experimental parameters associated with the response of an interferometer in the presence of a gravitational potential from a proof mass. We consider a proof mass with nonzero 3D thickness, rather than the 1D ring proof mass of Sec. IV B. Computing higher-order quantum corrections to proof mass potentials using Eq. 15 can be challenging in a physical parameter space because the Gaussian over which proof mass potential is convolved can be narrow relative to the span of the potential along the interferometer axis. For instance, with $w_0 = 10 \mu\text{m}$, $t = 2.8$ s, and $\hbar/m = 7.25 \times 10^{-10} \text{ m}^2/\text{s}$, the standard deviation of the Gaussian is $\sigma = \frac{1}{2} \sqrt{w_0^2 + \frac{4\hbar^2 t^2}{m^2 w_0^2}} \approx 0.2$ mm, which is small compared to meter-scale span of the proof mass potential. The semi-classical approximation takes the limit that the Gaussian over which the potential is convolved is a delta function (see Equations 15 and 16). Quantum corrections are encoded in the small but finite width of this Gaussian. It is computationally expensive to reliably evaluate quantum corrections by numerically evaluating the convolution integral owing to the large grid sampling

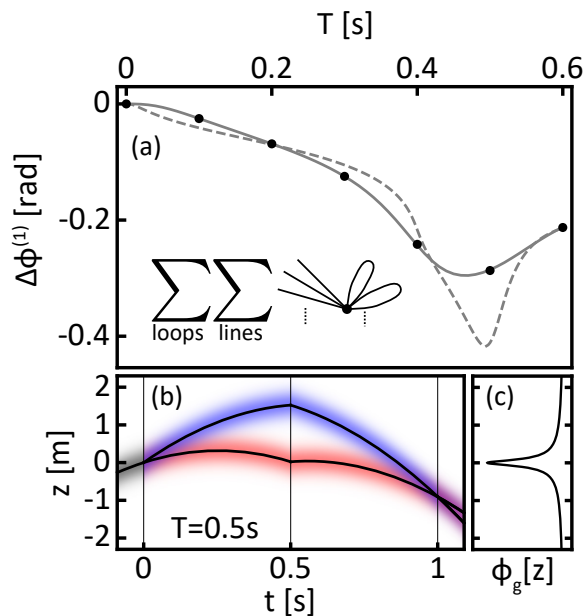


FIG. 5. Simulation of phase shift from proof mass potential. (a) The numerically evaluated interferometer phase as a function of the interrogation time T (black points), superimposed with the phase shifts as computed via the semi-classical method (dashed gray line, Eq. 16) and the diagrammatic method (solid gray line, Eq. 15). The diagrammatic solution comes from evaluating the sum over an infinite number of 1-vertex diagrams, as indicated by the expression in the left hand side. (b) The two arms of the interferometer for a $T = 0.5$ s sequence. The black lines denote the classical trajectories and the red and blue density plots denote the wavepackets associated with the two interferometer arms. (c) The form of the proof mass potential (Eq. 17), for reference against the arm trajectories. The calculations are performed using the following parameters (in SI units): $w_0 = 0.5$, $\hbar/m = 10^{-2}$, $v_z = 2.5$, $v_r = 3$, $g = 10$, $GM = 10^{-3}$, $R = 7 \times 10^{-2}$, $\Delta z = 1.25 \times 10^{-3}$, $\Delta t = 2.5 \times 10^{-4}$.

required by the large span of the proof mass potential, and the fine grid resolution required by the narrow Gaussian. A more productive approach is to evaluate Eq. 15 analytically order by order in σ , then integrate each term numerically in time. This approach is akin to using Eq. 14 to evaluate the corrections, where $k = 0$ corresponds to the semi-classical case, and $k \geq 1$ terms contain the quantum corrections. In this parameter space, the contributions for larger values of k , which encode higher-order quantum corrections, decrease as k increases. In Fig. 6, the quantum correction to the interferometer phase shift is displayed as a function of the initial wavepacket waist w_0 and associated atom cloud temperature, along with a cartoon of the proof mass used to generate the potential. The vertical vacuum tube, whose axis of cylindrical symmetry is co-linear with the interferometer axis (the z axis), has a 15 cm outer diameter. The proof mass is a hollow cylinder with the density of Tungsten, an internal radius of 0.08 m, an external radius of 0.5 m, and a

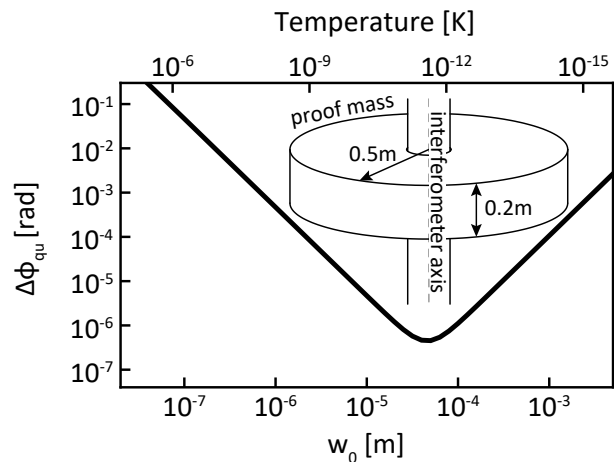


FIG. 6. Estimate of quantum corrections to interferometer phase shift to first order in the proof mass potential for a ≈ 2933 kg proof mass. It is assumed that the interferometer has a 100 photon recoil momentum splitting, $T \approx 1.40$ s, and $v_z \approx 13.35$ m/s. We take the interferometer to operate on the 698 nm clock transition of ^{87}Sr . The first order semi-classical contribution from just the proof masses is ≈ 235 rad. The relationship between temperature and beam waist is taken to be $w_0 = \hbar/\sqrt{mk_B T_K}$, where m is the mass of the strontium atom, k_B is Boltzmann's constant and T_K is the cloud temperature. A 0.15 m outer diameter vacuum tube is indicated for reference. The inner diameter of the proof mass is 0.16m and the position of the center of the proof mass is 0.2 m below the apex of the upper interferometer arm's trajectory along the interferometer axis. The axis of the interferometer, z , is indicated in the dashed gray line.

height of 0.2 m. The quantum corrections to the phase shift, $\Delta\phi_{\text{qu}}$, are computed by evaluating the terms of Eq. 14 from $k = 1$ to $k = 3$ by taking derivatives of the analytic form of the thick proof mass potential and integrating numerically in time. For certain values of w_0 , the scale of these quantum corrections can be $> \text{mrad}$, which could be measurable. This result indicates that quantum corrections to the phase shift might need to be considered for gravitational experiments with proof masses, including precision measurements of Newton's gravitational constant G or searches for fifth forces.

V. OUTLOOK

We have introduced a new formalism for analytically calculating quantum corrections to the traditional semi-classical approximations used to analyze matter wave interferometers. We have applied this formalism to examples involving anharmonic traps and gravitational potentials from a local proof mass, and demonstrated that these quantum corrections can be significant for realistic experimental parameters. It could therefore be important to consider and account for their effects in future measurements.

In future work, this diagrammatic calculator can be extended to more than one spatial dimension, where edges and vertices pick up additional labels associated with the additional spatial dimensions. Moreover, it could be productive to investigate the application of this approach to rotating frames of reference, in which Coriolis forces emerge, leading to terms in the Lagrangian that couple position and momentum operators. The generalization of the calculation to non-Gaussian initial wavepackets is another direction for future study. Corrections to the interferometer phase that are higher than first order in an external potential with arbitrary spatial dependence can also be evaluated by summing over the infinite number of 2-vertex diagrams in the same manner as was done in Sec. IV C. In this case, the two-vertex diagrams can be parametrized in by five parameters: the number of external edges and loops on one vertex, the number of external edges and loops on the other, and the number of internal edges between them. Then a sum can be performed over the five parameters to arrive at an analytic expression for the phase shift at second order in the arbitrary potential. In addition to computing interferometer phase shifts, this formalism could also be applied to computing perturbative corrections to matter

wavepackets themselves as they evolve in anharmonic potentials. Furthermore, owing to the structural similarity of the free particle Schrodinger equation and the paraxial wave equation, this formalism could prove useful for generating analytic expressions for the profiles of Gaussian laser beams propagating with small aberrations.

VI. ACKNOWLEDGEMENTS

We thank Cass Sackett and Michael Kagan for valuable discussions. This material is based upon work supported by the U.S. Department of Energy, Office of Science, National Quantum Information Science Research Centers, Superconducting Quantum Materials and Systems Center (SQMS) under contract number DE-AC02-07CH11359. This work is funded in part by the Gordon and Betty Moore Foundation (Grant GBMF7945), the David and Lucile Packard Foundation (Fellowship for Science and Engineering), and the Office of Naval Research (Grant Number N00014-19-1-2181). JG acknowledges support from a National Science Foundation (NSF) Quantum Information Science and Engineering Network (QISE-NET) Graduate Fellowship, funded by NSF award No. DMR-1747426.

-
- [1] A. D. Cronin, J. Schmiedmayer, and D. E. Pritchard, Optics and interferometry with atoms and molecules, *Rev. Mod. Phys.* **81**, 1051 (2009).
- [2] A. Peters, K. Y. Chung, and S. Chu, High-precision gravity measurements using atom interferometry, *Metrologia* **38**, 25 (2001).
- [3] J. M. McGuirk, G. T. Foster, J. B. Fixler, M. J. Snadden, and M. A. Kasevich, Sensitive absolute-gravity gradiometry using atom interferometry, *Phys. Rev. A* **65**, 033608 (2002).
- [4] D. S. Durfee, Y. K. Shaham, and M. A. Kasevich, Long-term stability of an area-reversible atom-interferometer sagnac gyroscope, *Phys. Rev. Lett.* **97**, 240801 (2006).
- [5] X. Wu, Z. Pagel, B. S. Malek, T. H. Nguyen, F. Zi, D. S. Scheirer, and H. Müller, Gravity surveys using a mobile atom interferometer, *Sci. Adv.* **5**, eaax0800 (2019).
- [6] K. Bongs, M. Holynski, J. Vovrosh, P. Bouyer, G. Condon, E. Rasel, C. Schubert, W. P. Schleich, and A. Roura, Taking atom interferometric quantum sensors from the laboratory to real-world applications, *Nat. Rev. Phys.* **1**, 731 (2019).
- [7] Y. Bidel, N. Zahzam, A. Bresson, C. Blanchard, M. Cadoret, A. V. Olesen, and R. Forsberg, Absolute airborne gravimetry with a cold atom sensor, *Journal of Geodesy* **94**, 20 (2020).
- [8] B. Canuel, A. Bertoldi, L. Amand, E. Pozzo di Borgo, T. Chantrait, C. Danquigny, M. Dovale Álvarez, B. Fang, A. Freise, R. Geiger, J. Gillot, S. Henry, J. Hinderer, D. Holleville, J. Junca, G. Lefèvre, M. Merzougui, N. Mielec, T. Monfret, S. Pelisson, M. Prevedelli, S. Reynaud, I. Riou, Y. Rogister, S. Rosat, E. Cormier, A. Landragin, W. Chaibi, S. Gaffet, and P. Bouyer, Exploring gravity with the miga large scale atom interferometer, *Scientific Reports* **8**, 14064 (2018).
- [9] K. Bongs, R. Launay, and M. A. Kasevich, High-order inertial phase shifts for time-domain atom interferometers, *Applied Physics B* **84**, 599 (2006).
- [10] J. K. Stockton, K. Takase, and M. A. Kasevich, Absolute geodetic rotation measurement using atom interferometry, *Phys. Rev. Lett.* **107**, 133001 (2011).
- [11] G. W. Biedermann, X. Wu, L. Deslauriers, S. Roy, C. Mahadeswaraswamy, and M. A. Kasevich, Testing gravity with cold-atom interferometers, *Phys. Rev. A* **91**, 033629 (2015).
- [12] S. Fray, C. A. Diez, T. W. Hänsch, and M. Weitz, Atomic interferometer with amplitude gratings of light and its applications to atom based tests of the equivalence principle, *Phys. Rev. Lett.* **93**, 240404 (2004).
- [13] D. Schlippert, J. Hartwig, H. Albers, L. L. Richardson, C. Schubert, A. Roura, W. P. Schleich, W. Ertmer, and E. M. Rasel, Quantum test of the universality of free fall, *Phys. Rev. Lett.* **112**, 203002 (2014).
- [14] L. Zhou, S. Long, B. Tang, X. Chen, F. Gao, W. Peng, W. Duan, J. Zhong, Z. Xiong, J. Wang, Y. Zhang, and M. Zhan, Test of equivalence principle at 10^{-8} level by a dual-species double-diffraction raman atom interferometer, *Phys. Rev. Lett.* **115**, 013004 (2015).
- [15] C. C. N. Kuhn, G. D. McDonald, K. S. Hardman, S. Bennetts, P. J. Everitt, P. A. Altin, J. E. Debs, J. D. Close, and N. P. Robins, A bose-condensed, simultaneous dual-species mach-zehnder atom interferometer, *New Journal of Physics* **16**, 073035 (2014).
- [16] M. G. Tarallo, T. Mazzoni, N. Poli, D. V. Sutyryn, X. Zhang, and G. M. Tino, Test of einstein equivalence

- principle for 0-spin and half-integer-spin atoms: Search for spin-gravity coupling effects, *Phys. Rev. Lett.* **113**, 023005 (2014).
- [17] A. Bonnin, N. Zahzam, Y. Bidel, and A. Bresson, Simultaneous dual-species matter-wave accelerometer, *Phys. Rev. A* **88**, 043615 (2013).
- [18] J. Hartwig, S. Abend, C. Schubert, D. Schlippert, H. Ahlers, K. Posso-Trujillo, N. Gaaloul, W. Ertmer, and E. M. Rasel, Testing the universality of free fall with rubidium and ytterbium in a very large baseline atom interferometer, *New Journal of Physics* **17**, 035011 (2015).
- [19] P. Asenbaum, C. Overstreet, M. Kim, J. Curti, and M. A. Kasevich, Atom-interferometric test of the equivalence principle at the 10^{-12} level, *Phys. Rev. Lett.* **125**, 191101 (2020).
- [20] J. Williams, S. wey Chiow, N. Yu, and H. Müller, Quantum test of the equivalence principle and space-time aboard the international space station, *New Journal of Physics* **18**, 025018 (2016).
- [21] B. Battelier, J. Bergé, A. Bertoldi, L. Blanchet, K. Bongs, P. Bouyer, C. Braxmaier, D. Calonico, P. Fayet, N. Gaaloul, C. Guerlin, A. Hees, P. Jetzer, C. Lämmerzahl, S. Lecomte, C. Le Poncin-Lafitte, S. Loriani, G. Métris, M. Nofrarias, E. Rasel, S. Reynaud, M. Rodrigues, M. Rothacher, A. Roura, C. Salomon, S. Schiller, W. P. Schleich, C. Schubert, C. F. Sopuerta, F. Sorrentino, T. J. Sumner, G. M. Tino, P. Tuckey, W. v. Klitzing, L. Wörner, P. Wolf, and M. Zelan, Exploring the foundations of the physical universe with space tests of the equivalence principle, *Experimental Astronomy* **51**, 1695–1736 (2021).
- [22] G. Rosi, G. D’Amico, L. Cacciapuoti, F. Sorrentino, M. Prevedelli, M. Zych, Č. Brukner, and G. M. Tino, Quantum test of the equivalence principle for atoms in coherent superposition of internal energy states, *Nature Communications* **8**, 15529 (2017).
- [23] B. Barrett, L. Antoni-Micollier, L. Chichet, B. Battelier, T. Lévêque, A. Landragin, and P. Bouyer, Dual matter-wave inertial sensors in weightlessness, *Nature Communications* **7**, 13786 (2016).
- [24] J. G. Wacker, Using atom interferometry to search for new forces, *Physics Letters B* **690**, 38 (2010).
- [25] J. B. Fixler, G. T. Foster, J. M. McGuirk, and M. A. Kasevich, Atom interferometer measurement of the newtonian constant of gravity, *Science* **315**, 74 (2007), <https://www.science.org/doi/pdf/10.1126/science.1135459>.
- [26] G. Rosi, F. Sorrentino, L. Cacciapuoti, M. Prevedelli, and G. M. Tino, Precision measurement of the newtonian gravitational constant using cold atoms, *Nature* **510**, 518 (2014).
- [27] G. Lamporesi, A. Bertoldi, L. Cacciapuoti, M. Prevedelli, and G. M. Tino, Determination of the newtonian gravitational constant using atom interferometry, *Phys. Rev. Lett.* **100**, 050801 (2008).
- [28] R. H. Parker, C. Yu, W. Zhong, B. Estey, and H. Müller, Measurement of the fine-structure constant as a test of the standard model, *Science* **360**, 191 (2018), <https://www.science.org/doi/pdf/10.1126/science.aap7706>.
- [29] R. Bouchendira, P. Cladé, S. Guellati-Khélifa, F. m. c. Nez, and F. m. c. Biraben, New determination of the fine structure constant and test of the quantum electrodynamics, *Phys. Rev. Lett.* **106**, 080801 (2011).
- [30] P. Hamilton, M. Jaffe, P. Haslinger, Q. Simmons, H. Müller, and J. Khoury, Atom-interferometry constraints on dark energy, *Science* **349**, 849 (2015), <https://www.science.org/doi/pdf/10.1126/science.aaa8883>.
- [31] S.-w. Chiow and N. Yu, Multiloop atom interferometer measurements of chameleon dark energy in microgravity, *Physical Review D* **97**, 044043 (2018).
- [32] A. Arvanitaki, P. W. Graham, J. M. Hogan, S. Rajendran, and K. Van Tilburg, Search for light scalar dark matter with atomic gravitational wave detectors, *Phys. Rev. D* **97**, 075020 (2018).
- [33] Y. A. El-Neaj, C. Alpigiani, S. Amairi-Pyka, H. Araújo, A. Balaž, A. Bassi, L. Bathe-Peters, B. Battelier, A. Belić, E. Bentine, J. Bernabeu, A. Bertoldi, R. Bingham, D. Blas, V. Bolpasi, K. Bongs, S. Bose, P. Bouyer, T. Bowcock, W. Bowden, O. Buchmueller, C. Burrage, X. Calmet, B. Canuel, L.-I. Caramete, A. Carroll, G. Cella, V. Charmandaris, S. Chattopadhyay, X. Chen, M. L. Chiofalo, J. Coleman, J. Cotter, Y. Cui, A. Derevianko, A. De Roeck, G. S. Djordjevic, P. Dornan, M. Doser, I. Drougkakis, J. Dunningham, I. Dutan, S. Easo, G. Elertas, J. Ellis, M. El Sawy, F. Fassi, D. Felea, C.-H. Feng, R. Flack, C. Foot, I. Fuentes, N. Gaaloul, A. Gauguet, R. Geiger, V. Gibson, G. Giudice, J. Goldwin, O. Grachov, P. W. Graham, D. Grasso, M. van der Grinten, M. Gündogan, M. G. Haehnelt, T. Harte, A. Hees, R. Hobson, J. Hogan, B. Holst, M. Holynski, M. Kasevich, B. J. Kavanagh, W. von Klitzing, T. Kovachy, B. Krikler, M. Krutzik, M. Lewicki, Y.-H. Lien, M. Liu, G. G. Luciano, A. Magnon, M. A. Mahmoud, S. Malik, C. McCabe, J. Mitchell, J. Pahl, D. Pal, S. Pandey, D. Papazoglou, M. Paternostro, B. Penning, A. Peters, M. Prevedelli, V. Puthiya-Veettil, J. Quenby, E. Rasel, S. Ravenhall, J. Ringwood, A. Roura, D. Sabulsky, M. Sameed, B. Sauer, S. A. Schäffer, S. Schiller, V. Schkolnik, D. Schlippert, C. Schubert, H. R. Sfar, A. Shayeghi, I. Shipsey, C. Signorini, Y. Singh, M. Soares-Santos, F. Sorrentino, T. Sumner, K. Tassis, S. Tentindo, G. M. Tino, J. N. Tinsley, J. Unwin, T. Valenzuela, G. Vasilakis, V. Vaskonen, C. Vogt, A. Webber-Date, A. Wenzlowski, P. Windpassinger, M. Woltmann, E. Yazgan, M.-S. Zhan, X. Zou, and J. Zupan, Aedge: Atomic experiment for dark matter and gravity exploration in space, *EPJ Quantum Technology* **7**, 10.1140/epjqt/s40507-020-0080-0 (2020).
- [34] P. W. Graham, D. E. Kaplan, J. Mardon, S. Rajendran, and W. A. Terrano, Dark matter direct detection with accelerometers, *Phys. Rev. D* **93**, 075029 (2016).
- [35] S. Abend, B. Allard, I. Alonso, J. Antoniadis, H. Araújo, G. Arduini, A. S. Arnold, T. Asano, N. Augst, L. Badurina, *et al.*, Terrestrial very-long-baseline atom interferometry: Workshop summary, *AVS Quantum Science* **6**, 024701 (2024).
- [36] P. W. Graham, D. E. Kaplan, J. Mardon, S. Rajendran, W. A. Terrano, L. Trahms, and T. Wilkason, Spin precession experiments for light axionic dark matter, *Phys. Rev. D* **97**, 055006 (2018).
- [37] F. Di Pumpo, A. Friedrich, and E. Giese, Optimal baseline exploitation in vertical dark-matter detectors based on atom interferometry, *AVS Quantum Science* **6** (2024).
- [38] M. Abe, P. Adamson, M. Borcean, D. Bortoletto, K. Bridges, S. P. Carman, S. Chattopadhyay, J. Cole-

- man, N. M. Curfman, K. DeRose, *et al.*, Matter-wave atomic gradiometer interferometric sensor (magis-100), *Quantum Sci. Technol.* **6**, 044003 (2021).
- [39] L. Badurina, E. Bentine, D. Blas, K. Bongs, D. Bortoletto, T. Bowcock, K. Bridges, W. Bowden, O. Buchmueller, C. Burrage, J. Coleman, G. Elert, J. Ellis, C. Foot, V. Gibson, M. Haehnel, T. Harte, S. Hedges, R. Hobson, M. Holynski, T. Jones, M. Langlois, S. Lelouch, M. Lewicki, R. Maiolino, P. Majewski, S. Malik, J. March-Russell, C. McCabe, D. Newbold, B. Sauer, U. Schneider, I. Shipsey, Y. Singh, M. Uchida, T. Valenzuela, M. van der Grinten, V. Vaskonen, J. Vosseveld, D. Weatherill, and I. Wilmot, Aion: an atom interferometer observatory and network, *Journal of Cosmology and Astroparticle Physics* **2020** (05), 011.
- [40] M.-S. Zhan, J. Wang, W.-T. Ni, D.-F. Gao, G. Wang, L.-X. He, R.-B. Li, L. Zhou, X. Chen, J.-Q. Zhong, B. Tang, Z.-W. Yao, L. Zhu, Z.-Y. Xiong, S.-B. Lu, G.-H. Yu, Q.-F. Cheng, M. Liu, Y.-R. Liang, P. Xu, X.-D. He, M. Ke, Z. Tan, and J. Luo, Zaiga: Zhaoshan long-baseline atom interferometer gravitation antenna, *International Journal of Modern Physics D* **29**, 1940005 (2020), <https://doi.org/10.1142/S0218271819400054>.
- [41] P. W. Graham, J. M. Hogan, M. A. Kasevich, and S. Rajendran, Resonant mode for gravitational wave detectors based on atom interferometry, *Phys. Rev. D* **94**, 104022 (2016).
- [42] A. Torres-Orjuela, Detecting intermediate-mass black hole binaries with atom interferometer observatories: Using the resonant mode for the merger phase, *AVS Quantum Science* **5** (2023).
- [43] Y. A. El-Neaj, C. Alpigiani, S. Amairi-Pyka, H. Araújo, A. Balaž, A. Bassi, L. Bathe-Peters, B. Battelier, A. Belić, E. Bentine, J. Bernabeu, A. Bertoldi, R. Bingham, *et al.*, AEDGE: Atomic Experiment for Dark Matter and Gravity Exploration in Space, *EPJ Quantum Technol.* **7**, 6 (2020).
- [44] S. Baum, Z. Bogorad, and P. W. Graham, Gravitational wave measurement in the mid-band with atom interferometers, *Journal of Cosmology and Astroparticle Physics* **2024** (05), 027.
- [45] C. Schubert, D. Schlippert, S. Abend, E. Giese, A. Roura, W. Schleich, W. Ertmer, and E. Rasel, Scalable, symmetric atom interferometer for infrasound gravitational wave detection, *arXiv preprint arXiv:1909.01951* (2019).
- [46] S. Dimopoulos, P. W. Graham, J. M. Hogan, M. A. Kasevich, and S. Rajendran, Atomic gravitational wave interferometric sensor, *Phys. Rev. D* **78**, 122002 (2008).
- [47] N. Yu and M. Tinto, Gravitational wave detection with single-laser atom interferometers, *General Relativity and Gravitation* **43**, 1943 (2011).
- [48] W. Chaibi, R. Geiger, B. Canuel, A. Bertoldi, A. Landragin, and P. Bouyer, Low frequency gravitational wave detection with ground-based atom interferometer arrays, *Phys. Rev. D* **93**, 021101 (2016).
- [49] J. M. Hogan, D. M. S. Johnson, S. Dickerson, T. Kovachy, A. Sugarbaker, S.-w. Chiow, P. W. Graham, M. A. Kasevich, B. Saif, S. Rajendran, P. Bouyer, B. D. Seery, L. Feinberg, and R. Keski-Kuha, An atomic gravitational wave interferometric sensor in low earth orbit (agis-leo), *General Relativity and Gravitation* **43**, 1953 (2011).
- [50] P. W. Graham, J. M. Hogan, M. A. Kasevich, and S. Rajendran, New method for gravitational wave detection with atomic sensors, *Phys. Rev. Lett.* **110**, 171102 (2013).
- [51] B. Canuel, S. Abend, P. Amaro-Seoane, F. Badaracco, Q. Beaufils, A. Bertoldi, K. Bongs, P. Bouyer, C. Braxmaier, W. Chaibi, N. Christensen, F. Fitzek, G. Flouris, N. Gaaloul, S. Gaffet, C. L. G. Alzar, R. Geiger, S. Guellati-Khelifa, K. Hammerer, J. Harms, J. Hinderer, M. Holynski, J. Junca, S. Katsanevas, C. Klempt, C. Kozanitis, M. Krutzik, A. Landragin, I. L. Roche, B. Leykauf, Y.-H. Lien, S. Loriani, S. Merlet, M. Merzougui, M. Nofrarias, P. Papadakos, F. P. dos Santos, A. Peters, D. Plexousakis, M. Prevedelli, E. M. Rasel, Y. Rogister, S. Rosat, A. Roura, D. O. Sabulsky, V. Schkolnik, D. Schlippert, C. Schubert, L. Sidorenkov, J.-N. Siemß, C. F. Sopaerta, F. Sorrentino, C. Struckmann, G. M. Tino, G. Tsagkatakis, A. Viceré, W. von Klitzing, L. Woerner, and X. Zou, Elgar—a european laboratory for gravitation and atom-interferometric research, *Classical and Quantum Gravity* **37**, 225017 (2020).
- [52] P. W. Graham, J. M. Hogan, M. A. Kasevich, S. Rajendran, and R. W. Romani, Mid-band gravitational wave detection with precision atomic sensors (2017), *arXiv:1711.02225 [astro-ph.IM]*.
- [53] A. Bassi, K. Lochan, S. Satin, T. P. Singh, and H. Ulbricht, Models of wave-function collapse, underlying theories, and experimental tests, *Rev. Mod. Phys.* **85**, 471 (2013).
- [54] S. Nimmrichter and K. Hornberger, Macroscopicity of mechanical quantum superposition states, *Phys. Rev. Lett.* **110**, 160403 (2013).
- [55] A. Bassi, A. Großardt, and H. Ulbricht, Gravitational decoherence, *Classical and Quantum Gravity* **34**, 193002 (2017).
- [56] N. Altamirano, P. Corona-Ugalde, R. B. Mann, and M. Zych, Gravity is not a pairwise local classical channel, *Classical and Quantum Gravity* **35**, 145005 (2018).
- [57] T. Kovachy, P. Asenbaum, C. Overstreet, C. A. Donnelly, S. M. Dickerson, A. Sugarbaker, J. M. Hogan, and M. A. Kasevich, Quantum superposition at the half-metre scale, *Nature* **528**, 530 (2015).
- [58] P. Asenbaum, C. Overstreet, T. Kovachy, D. D. Brown, J. M. Hogan, and M. A. Kasevich, Phase shift in an atom interferometer due to spacetime curvature across its wave function, *Phys. Rev. Lett.* **118**, 183602 (2017).
- [59] V. Xu, M. Jaffe, C. D. Panda, S. L. Kristensen, L. W. Clark, and H. Müller, Probing gravity by holding atoms for 20 seconds, *Science* **366**, 745 (2019), <https://www.science.org/doi/pdf/10.1126/science.aay6428>.
- [60] M. Arndt and K. Hornberger, Testing the limits of quantum mechanical superpositions, *Nature Physics* **10**, 271 (2014).
- [61] M. Zych, F. Costa, I. Pikovski, and Č. Brukner, Quantum interferometric visibility as a witness of general relativistic proper time, *Nature Communications* **2**, 505 (2011).
- [62] A. Roura, Gravitational redshift in quantum-clock interferometry, *Phys. Rev. X* **10**, 021014 (2020).
- [63] D. Carney, H. Müller, and J. M. Taylor, Using an atom interferometer to infer gravitational entanglement generation, *PRX Quantum* **2**, 030330 (2021).

- [64] C. Overstreet, P. Asenbaum, J. Curti, M. Kim, and M. A. Kasevich, Observation of a gravitational aharonov-bohm effect, *Science* **375**, 226 (2022), <https://www.science.org/doi/pdf/10.1126/science.abl7152>.
- [65] P. Storey and C. Cohen-Tannoudji, The Feynman path integral approach to atomic interferometry: A tutorial, *J. Phys. II* **4**, 1999 (1994).
- [66] J. M. Hogan, D. M. S. Johnson, and M. A. Kasevich, Light-pulse atom interferometry (2008), arXiv:0806.3261 [physics.atom-ph].
- [67] G. Tino and M. Kasevich, *Atom Interferometry: Proceedings of the International School of Physics "Enrico Fermi", Course 188, Varenna on Lake Como, Villa Monastero, 15-20 July 2013*, International School of Physics Enrico Fermi Series (IOS Press, 2014).
- [68] C. Antoine and C. J. Bordé, Quantum theory of atomic clocks and gravito-inertial sensors: an update, *Journal of Optics B: Quantum and Semiclassical Optics* **5**, S199 (2003).
- [69] C. Antoine and C. Bordé, Exact phase shifts for atom interferometry, *Physics Letters A* **306**, 277 (2003).
- [70] B. Dubetsky and M. Kasevich, Atom interferometer as a selective sensor of rotation or gravity, *Physical Review A—Atomic, Molecular, and Optical Physics* **74**, 023615 (2006).
- [71] Here we consider the recoil velocity kicks v_r the matter-wave receives from absorbing/emitting a photon to not explicitly include its dependence on \hbar through the photon momentum, see Tab. I.
- [72] F. Fitzek, J.-N. Siemß, S. Seckmeyer, H. Ahlers, E. M. Rasel, K. Hammerer, and N. Gaaloul, Universal atom interferometer simulation of elastic scattering processes, *Scientific Reports* **10** (2020).
- [73] B. Dubetsky, S. B. Libby, and P. Berman, Atom interferometry in the presence of an external test mass, *Atoms* **4**, 14 (2016).
- [74] A. Bertoldi, F. Minardi, and M. Prevedelli, Phase shift in atom interferometers: Corrections for nonquadratic potentials and finite-duration laser pulses, *Physical Review A* **99**, 033619 (2019).
- [75] R. E. Sapiro, R. Zhang, and G. Raithel, Atom interferometry using kapitza-dirac scattering in a magnetic trap, *Phys. Rev. A* **79**, 043630 (2009).
- [76] W. Hänsel, J. Reichel, P. Hommelhoff, and T. W. Hänsch, Trapped-atom interferometer in a magnetic microtrap, *Phys. Rev. A* **64**, 063607 (2001).
- [77] T. Schumm, P. Krüger, S. Hofferberth, I. Lesanovsky, S. Wildermuth, S. Groth, I. Bar-Joseph, L. M. Anderson, and J. Schmiedmayer, A double well interferometer on an atom chip, *Quantum Information Processing* **5**, 537 (2006).
- [78] M. M. Beydler, E. R. Moan, Z. Luo, Z. Chu, and C. A. Sackett, Guided-wave Sagnac atom interferometer with large area and multiple orbits, *AVS Quantum Science* **6**, 014401 (2024), <https://pubs.aip.org/avs/aqs/article-pdf/doi/10.1116/5.0173769/18292053/014401.1.5.0173769.pdf>.
- [79] M. Horikoshi and K. Nakagawa, Dephasing due to atom-atom interaction in a waveguide interferometer using a bose-einstein condensate, *Phys. Rev. A* **74**, 031602 (2006).
- [80] G. Raithel, A. Duspayev, B. Dash, S. C. Carrasco, M. H. Goerz, V. Vuletić, and V. S. Malinovsky, Principles of tractor atom interferometry, *Quantum Science and Technology* **8**, 014001 (2022).
- [81] B. Dash, M. H. Goerz, A. Duspayev, S. C. Carrasco, V. S. Malinovsky, and G. Raithel, Rotation sensing using tractor atom interferometry, *AVS Quantum Science* **6**, 014407 (2024), <https://pubs.aip.org/avs/aqs/article-pdf/doi/10.1116/5.0175802/19712564/014407.1.5.0175802.pdf>.
- [82] G. D. McDonald, C. C. N. Kuhn, S. Bennetts, J. E. Debs, K. S. Hardman, M. Johnsson, J. D. Close, and N. P. Robins, $80\hbar k$ momentum separation with bloch oscillations in an optically guided atom interferometer, *Phys. Rev. A* **88**, 053620 (2013).
- [83] G. D. McDonald, H. Keal, P. A. Altin, J. E. Debs, S. Bennetts, C. C. N. Kuhn, K. S. Hardman, M. T. Johnsson, J. D. Close, and N. P. Robins, Optically guided linear mach-zehnder atom interferometer, *Phys. Rev. A* **87**, 013632 (2013).
- [84] K. A. Krzyzanowska, J. Ferreras, C. Ryu, E. C. Samson, and M. G. Boshier, Matter-wave analog of a fiber-optic gyroscope, *Phys. Rev. A* **108**, 043305 (2023).
- [85] H. Kim, K. Krzyzanowska, K. C. Henderson, C. Ryu, E. Timmermans, and M. Boshier, One second interrogation time in a 200 round-trip waveguide atom interferometer (2022), arXiv:2201.11888 [physics.atom-ph].
- [86] R. Charrière, M. Cadoret, N. Zahzam, Y. Bidel, and A. Bresson, Local gravity measurement with the combination of atom interferometry and bloch oscillations, *Phys. Rev. A* **85**, 013639 (2012).
- [87] C. D. Panda, M. J. Tao, M. Ceja, J. Khoury, G. M. Tino, and H. Müller, Measuring gravitational attraction with a lattice atom interferometer, *Nature* 10.1038/s41586-024-07561-3 (2024).
- [88] C. D. Panda, M. Tao, J. Egelhoff, M. Ceja, V. Xu, and H. Müller, Coherence limits in lattice atom interferometry at the one-minute scale, *Nature Physics* 10.1038/s41567-024-02518-9 (2024).
- [89] T. Kovachy, J. M. Hogan, D. M. S. Johnson, and M. A. Kasevich, Optical lattices as waveguides and beam splitters for atom interferometry: An analytical treatment and proposal of applications, *Phys. Rev. A* **82**, 013638 (2010).
- [90] C. D. Panda, M. Tao, M. Ceja, A. Reynoso, and H. Müller, Atomic gravimeter robust to environmental effects, *Applied Physics Letters* **123** (2023).
- [91] M. Feit, J. Fleck, and A. Steiger, Solution of the schrödinger equation by a spectral method, *Journal of Computational Physics* **47**, 412 (1982).
- [92] M. Srednicki, *Quantum field theory* (Cambridge University Press, 2007).
- [93] A. Zee, *Quantum Field Theory in a Nutshell: Second Edition*, In a Nutshell (Princeton University Press, 2010).
- [94] M. Peskin, *An Introduction To Quantum Field Theory* (CRC Press, 2018).
- [95] R. Feynman and A. Hibbs, *Quantum Mechanics and Path Integrals*, International Earth and Planetary Sciences Series (McGraw-Hill, 1965).
- [96] This follows from the fact that $\psi^{(0)}$ is a convolution of ψ_0 and $K^{(0)}$, which are both Gaussian. Convolution of two Gaussians is equivalent to taking the inverse Fourier transform of the product of the Fourier transform of the two Gaussians. Since the Fourier transform of a Gaussian is Gaussian, and the product of two Gaussians is Gaussian, $\psi^{(0)}$ must be Gaussian.

- [97] J. H. T. Burke and C. A. Sackett, Scalable bose-einstein-condensate sagnac interferometer in a linear trap, *Phys. Rev. A* **80**, 061603 (2009).
- [98] E. R. Moan, S. J. Berl, Z. Luo, and C. Sackett, Controlling the anharmonicity of a time-orbiting potential trap, in *OPTO* (2020).
- [99] As described in [78], an upgraded version of this apparatus has been implemented with reduced anharmonicities.
- [100] E. Moan, Z. Luo, and C. A. Sackett, A large-area Sagnac interferometer using atoms in a time-orbiting potential, in *Optical, Opto-Atomic, and Entanglement-Enhanced Precision Metrology*, Vol. 10934, edited by S. M. Shahriar and J. Scheuer, International Society for Optics and Photonics (SPIE, 2019) p. 109341X.
- [101] I. Hirschman and D. Widder, *The Convolution Transform*, Dover Books on Mathematics (Dover Publications, 2012).

Appendix A: Calculating Value of Diagram External and Internal Edges

To compute the value of diagram edges, it will be important to leverage two Gaussian integral identities, denoted as Eq. A1 and Eq. A2. Both of these integral identities are ultimately just extensions of the identity $\int_{-\infty}^{\infty} dx e^{-ax^2+bx} = \sqrt{\pi/a} e^{b^2/(4a)}$ for $\text{Re}[a] > 0$. The first integral identity is

$$I_1[x] = A \exp \left[x^2 G^{(0,2)} + x G^{(0,1)} + G^{(0,0)} + \int_{t_i}^{t_f} dt (x G^{(1,1)}[t] + G^{(1,0)}[t]) J[t] + \frac{1}{2} \int_{t_i}^{t_f} dt_1 \int_{t_i}^{t_f} dt_2 J[t_1] G^{(2,0)}[t_1, t_2] J[t_2] \right]$$

$$\int_{-\infty}^{\infty} dx I_1[x] = \bar{A} \exp \left[\bar{G}^{(0)} + \int_{t_i}^{t_f} dt \bar{G}^{(1)}[t] J[t] + \frac{1}{2} \int_{t_i}^{t_f} dt_1 \int_{t_i}^{t_f} dt_2 J[t_1] \bar{G}^{(2)}[t_1, t_2] J[t_2] \right]$$
(A1)

where

$$\bar{A} = A \sqrt{\frac{\pi}{-G^{(0,2)}}}$$

$$\bar{G}^{(0)} = G^{(0,0)} - \frac{(G^{(0,1)})^2}{4G^{(0,2)}}$$

$$\bar{G}^{(1)}[t] = G^{(1,0)}[t] - \frac{G^{(0,1)}G^{(1,1)}[t]}{2G^{(0,2)}}$$

$$\bar{G}^{(2)}[t_1, t_2] = G^{(2,0)}[t_1, t_2] - \frac{G^{(1,1)}[t_1]G^{(1,1)}[t_2]}{2G^{(0,2)}}$$

and $G^{(j,k)}[t_1, t_2]$ denotes a function associated with a term in the exponent of the integrand which is j^{th} order in the integration variable x and k^{th} order in the function $J[t]$. The second integral identity concerns integrating over an expression which consists of two different source terms J_1 and J_2 :

$$I_2[x] = A \exp \left[x^2 G^{(0,2)} + x G^{(0,1)} + G^{(0,0)} + \int_{t_i}^{t_f} dt \left((x G_1^{(1,1)}[t] + G_1^{(1,0)}[t]) J_1[t] + (x G_2^{(1,1)}[t] + G_2^{(1,0)}[t]) J_2[t] \right) \right.$$

$$\left. + \frac{1}{2} \int_{t_i}^{t_f} dt_1 \int_{t_i}^{t_f} dt_2 (J_1[t_1] G_{11}^{(2,0)}[t_1, t_2] J_1[t_2] + J_2[t_1] G_{22}^{(2,0)}[t_1, t_2] J_2[t_2]) \right]$$

$$\int_{-\infty}^{\infty} dx I_2[x] = \bar{A} \exp \left[\bar{G}^{(0)} + \int_{t_i}^{t_f} dt (\bar{G}_1^{(1)}[t] J_1[t] + \bar{G}_2^{(1)}[t] J_2[t]) \right.$$

$$\left. + \frac{1}{2} \int_{t_i}^{t_f} dt_1 \int_{t_i}^{t_f} dt_2 (J_1[t_1] \bar{G}_{11}^{(2)}[t_1, t_2] J_1[t_2] + J_1[t_1] \bar{G}_{12}^{(2)}[t_1, t_2] J_2[t_2] + J_2[t_1] \bar{G}_{21}^{(2)}[t_1, t_2] J_1[t_2] + J_2[t_1] \bar{G}_{22}^{(2)}[t_1, t_2] J_2[t_2]) \right]$$
(A2)

where

$$\begin{aligned}
\bar{A} &= A\sqrt{\frac{\pi}{-G^{(0,2)}}} \\
\bar{G}^{(0)} &= G^{(0,0)} - \frac{(G^{(0,1)})^2}{4G^{(0,2)}} \\
\bar{G}_j^{(1)}[t] &= G_j^{(1,0)}[t] - \frac{G^{(0,1)}G_j^{(1,1)}[t]}{2G^{(0,2)}} \quad , \quad j = 1, 2 \\
\bar{G}_{jk}^{(2)}[t_1, t_2] &= \delta_{jk}G_{jj}^{(2,0)}[t_1, t_2] - \frac{G_j^{(1,1)}[t_1]G_k^{(1,1)}[t_2]}{2G^{(0,2)}} \quad , \quad j, k = 1, 2
\end{aligned}$$

We will use both these expressions to compute the value of the internal and external edges associated with a diagram. Consider the Lagrangian

$$L = \frac{1}{2}\dot{x}^2 - \frac{1}{2}m\omega^2x^2 + J[t]x$$

for which a kernel solution can be written as [95]

$$\begin{aligned}
K^{(0)}[x_f, t_f; x_i, t_i; J[t]] &= \left(\frac{m\omega}{2\pi i \hbar \sin[\omega(t_f - t_i)]} \right)^{1/2} \\
&\times \exp \left[\frac{i}{\hbar} \frac{m\omega}{2 \sin[\omega(t_f - t_i)]} \left((x_f^2 + x_i^2) \cos[\omega(t_f - t_i)] - 2x_f x_i \right. \right. \\
&\quad \left. \left. + \frac{2}{m\omega} \int_{t_i}^{t_f} dt J[t] (x_f \sin[\omega(t - t_i)] + x_i \sin[\omega(t_f - t)]) \right. \right. \\
&\quad \left. \left. - \frac{1}{m^2\omega^2} \int_{t_i}^{t_f} dt_1 \int_{t_i}^{t_f} dt_2 J[t_1] J[t_2] \begin{cases} \sin[\omega(t_f - t_2)] \sin[\omega(t_1 - t_i)] & , t_1 < t_2 \\ \sin[\omega(t_f - t_1)] \sin[\omega(t_2 - t_i)] & , t_1 > t_2 \end{cases} \right) \right]
\end{aligned}$$

Defining an initial wavefunction of the form

$$\psi_0[x_i, t_i] = \left(\frac{2}{\pi w_0^2} \right)^{1/4} e^{-\frac{1}{2w_0^2}x_i^2}$$

Then the wavefunction at a later time t_f can be expressed as

$$\psi[x_f, t_f; J[t]] = \int_{-\infty}^{\infty} dx_i K[x_f, t_f; x_i, t_i; J[t]] \psi_0[x_i, t_i]$$

which can be solved by leveraging Eq. A1 with

$$\begin{aligned}
A &= \left(\frac{m\omega}{2\pi i \hbar \sin[\omega(t_f - t_i)]} \right)^{1/2} \left(\frac{2}{\pi w_0^2} \right)^{1/4} \\
G^{(0,2)} &= \frac{im\omega \cos[\omega(t_f - t_i)]}{2\hbar \sin[\omega(t_f - t_i)]} - \frac{1}{w_0^2} \\
G^{(0,1)} &= \frac{-im\omega x_f}{\hbar \sin[\omega(t_f - t_i)]} \\
G^{(0,0)} &= \frac{im\omega \cos[\omega(t_f - t_i)]x_f^2}{2\hbar \sin[\omega(t_f - t_i)]} \\
G^{(1,1)}[t] &= \frac{i \sin[\omega(t_f - t)]}{\hbar \sin[\omega(t_f - t_i)]} \\
G^{(1,0)}[t] &= \frac{i \sin[\omega(t - t_i)]x_f}{\hbar \sin[\omega(t_f - t_i)]} \\
G^{(2,0)}[t_1, t_2] &= \frac{-i}{m\omega \hbar \sin[\omega(t_f - t_i)]} \begin{cases} \sin[\omega(t_f - t_2)] \sin[\omega(t_1 - t_i)] & , t_1 < t_2 \\ \sin[\omega(t_f - t_1)] \sin[\omega(t_2 - t_i)] & , t_1 > t_2 \end{cases}
\end{aligned}$$

which results in

$$\psi[x_f, t_f; J[t]] = A_\psi \exp \left[x_f^2 G_\psi^{(0)} + x_f \int_{t_i}^{t_f} dt G_\psi^{(1)}[t] J[t] + \frac{1}{2} \int_{t_i}^{t_f} dt_1 \int_{t_i}^{t_f} dt_2 J[t_1] G_\psi^{(2)}[t_1, t_2] J[t_2] \right]$$

where

$$\begin{aligned} A_\psi &= \left(\frac{2}{\pi w_0^2} \right)^{1/4} \left(\frac{\omega}{\omega \cos[\omega(t_f - t_i)] + i\beta \sin[\omega(t_f - t_i)]} \right)^{1/2} \\ G_\psi^{(0)} &= -\frac{m\omega}{2\hbar} \frac{i\omega \sin[\omega(t_f - t_i)] + \beta \cos[\omega(t_f - t_i)]}{i\beta \sin[\omega(t_f - t_i)] + \omega \cos[\omega(t_f - t_i)]} \\ G_\psi^{(1)}[t] &= \frac{i}{\hbar} \left(\frac{\sin[\omega(t - t_i)]}{\sin[\omega(t_f - t_i)]} + \frac{\omega}{\omega \cos[\omega(t_f - t_i)] + i\beta \sin[\omega(t_f - t_i)]} \frac{\sin[\omega(t_f - t)]}{\sin[\omega(t_f - t_i)]} \right) \\ G_\psi^{(2)}[t_1, t_2] &= -\frac{1}{m\hbar} \left(\frac{i}{\omega \sin[\omega(t_f - t_i)]} \begin{cases} \sin[\omega(t_f - t_2)] \sin[\omega(t_1 - t_i)] & , t_1 < t_2 \\ \sin[\omega(t_f - t_1)] \sin[\omega(t_2 - t_i)] & , t_1 > t_2 \end{cases} \right. \\ &\quad \left. + \frac{1}{\beta \sin[\omega(t_f - t_i)] - i\omega \cos[\omega(t_f - t_i)]} \frac{\sin[\omega(t_f - t_1)] \sin[\omega(t_f - t_2)]}{\sin[\omega(t_f - t_i)]} \right) \end{aligned}$$

and $\beta = \frac{2\hbar}{mw_0^2}$. This is the integration done as part of Eq. 5 in the main text. Next we compute the expression

$$C e^{i\Delta\phi} = \int_{-\infty}^{\infty} dx_f \psi^{(0)}[x_f, t_f; J_1[t]] (\psi^{(0)}[x_f, t_f; J_2[t]])^*$$

using Eq. A2 with

$$\begin{aligned} A &= |A_\psi|^2 \\ G^{(0,2)} &= G_\psi^{(0)} + (G_\psi^{(0)})^* \\ G^{(0,1)} &= G^{(0,0)} = 0 \\ G_1^{(1,0)}[t] &= G_2^{(1,0)}[t] = 0 \\ G_1^{(1,1)}[t] &= G_\psi^{(1)}[t] \\ G_2^{(1,1)}[t] &= (G_\psi^{(1)}[t])^* \\ G_{11}^{(2,0)}[t_1, t_2] &= G_\psi^{(2)}[t_1, t_2] \\ G_{22}^{(2,0)}[t_1, t_2] &= (G_\psi^{(2)}[t_1, t_2])^* \end{aligned}$$

which results in

$$\begin{aligned} C e^{i\Delta\phi} = \exp \left[\frac{1}{2} \int_{t_i}^{t_f} dt_1 \int_{t_i}^{t_f} dt_2 \left(\right. & J_1[t_1] G_{11}[t_1, t_2] J_1[t_2] \\ & + J_1[t_1] G_{12}[t_1, t_2] J_2[t_2] \\ & + J_2[t_1] G_{21}[t_1, t_2] J_1[t_2] \\ & \left. + J_2[t_1] G_{22}[t_1, t_2] J_2[t_2] \right) \right] \end{aligned} \quad (\text{A3})$$

with

$$\begin{aligned}
G_{11}^{(2)}[t_1, t_2] &= \frac{1}{2m\hbar} \left(-\frac{\beta \sin[\omega(t_1 - t_i)] \sin[\omega(t_2 - t_i)]}{\omega^2} - \frac{\cos[\omega(t_1 - t_i)] \cos[\omega(t_2 - t_i)]}{\beta} + i \frac{\sin[\omega|t_1 - t_2|]}{\omega} \right) \\
G_{12}[t_1, t_2] &= \frac{1}{2m\hbar} \left(\frac{\beta \sin[\omega(t_1 - t_i)] \sin[\omega(t_2 - t_i)]}{\omega^2} + \frac{\cos[\omega(t_1 - t_i)] \cos[\omega(t_2 - t_i)]}{\beta} + i \frac{\sin[\omega(t_1 - t_2)]}{\omega} \right) \\
G_{21}[t_1, t_2] &= \frac{1}{2m\hbar} \left(\frac{\beta \sin[\omega(t_1 - t_i)] \sin[\omega(t_2 - t_i)]}{\omega^2} + \frac{\cos[\omega(t_1 - t_i)] \cos[\omega(t_2 - t_i)]}{\beta} - i \frac{\sin[\omega(t_1 - t_2)]}{\omega} \right) \\
G_{22}^{(2)}[t_1, t_2] &= \frac{1}{2m\hbar} \left(-\frac{\beta \sin[\omega(t_1 - t_i)] \sin[\omega(t_2 - t_i)]}{\omega^2} - \frac{\cos[\omega(t_1 - t_i)] \cos[\omega(t_2 - t_i)]}{\beta} - i \frac{\sin[\omega|t_1 - t_2|]}{\omega} \right)
\end{aligned}$$

In Sec. II B, we simplify the notation of Eq. A3 by expressing it as

$$C e^{i\Delta\phi} = \exp \left[\frac{1}{2} \int_{t_i}^{t_f} dt_1 \int_{t_i}^{t_f} dt_2 J_a[t_1] G_{ab}[t_1, t_2] J_b[t_2] \right]$$

where latin indices can have value 1 or 2 and summation over repeated indices is assumed. This is the integration that is done as part of Eq. 3 in the main text. Note that performing the integration this way results in $G_{ab}[t_j, t_k] = G_{ba}[t_k, t_j]$, which is a necessary symmetry of the propagator, akin to the property $G[x_1, x_2] = G[x_2, x_1]$ in QFT. To arrive at the expression for the propagators $G_{ab}[t_1, t_2]$ in Sec. III B, we take $t_i = 0$, and to arrive at the the propagators of Sec. III A we take the limit that $\omega \rightarrow 0$.

Now we compute the value of the external edge $G_a[t] = \int_{t_i}^{t_f} dt' J_{a'}[t'] G_{a'a}[t', t]$, which depends on the form of the effective force $J_a[t]$. In this paper, we consider two different pulse sequences, corresponding to two different choices of J_a : A Mach-Zehnder pulse sequence, as in Eq. 10

$$\frac{J_a[t]}{m} = -g + \begin{cases} v_r \delta[t - 0] - v_r \delta[t - T], & a = 1 \\ v_r \delta[t - T] - v_r \delta[t - 2T], & a = 2 \end{cases}$$

and a sequence where the two arms of the interferometer are kicked symmetrically as in Eq. 12.

$$\frac{J_a[t]}{m} = -g + \begin{cases} 2v_r \delta[t - 0] - 4v_r \delta[t - T] + 2v_r \delta[t - 2T] & a = 1 \\ -2v_r \delta[t - 0] + 4v_r \delta[t - T] - 2v_r \delta[t - 2T] & a = 2 \end{cases}$$

For the Mach Zehnder sequence, the value of the external edge $G_a[t]$ is given by

$$\begin{aligned}
G_1[t] &= \left(-\frac{2ig}{\hbar\omega^2} \right) \left(\sin[\omega t/2]^2 \right) + \left(\frac{iv_r}{2\hbar\omega} \right) \left(\sin[\omega|t|] + \sin[\omega(t - T)] - \sin[\omega|t - T|] - \sin[\omega(t - 2T)] \right) \\
&+ \left(\frac{iv_z}{2\hbar\omega} \right) \left(\sin[\omega t] + \sin[\omega|t|] \right) + \left(\frac{2v_r}{\hbar\beta} \right) \left(\cos[\omega t] \cos[\omega T] \sin[\omega T/2]^2 \right) + \left(\frac{2v_r\beta}{\hbar\omega^2} \right) \left(\sin[\omega t] \sin[\omega T] \sin[\omega T/2]^2 \right) \\
G_2[t] &= \left(\frac{2ig}{\hbar\omega^2} \right) \left(\sin[\omega t/2]^2 \right) + \left(-\frac{iv_r}{2\hbar\omega} \right) \left(\sin[\omega t] - \sin[\omega(t - T)] + \sin[\omega|t - T|] - \sin[\omega|t - 2T|] \right) \\
&+ \left(-\frac{iv_z}{2\hbar\omega} \right) \left(\sin[\omega t] + \sin[\omega|t|] \right) + \left(-\frac{2v_r}{\hbar\beta} \right) \left(\cos[\omega t] \cos[\omega T] \sin[\omega T/2]^2 \right) + \left(-\frac{2v_r\beta}{\hbar\omega^2} \right) \left(\sin[\omega t] \sin[\omega T] \sin[\omega T/2]^2 \right)
\end{aligned}$$

and for the symmetrically kicked sequence, external edges have value

$$\begin{aligned}
G_1[t] &= \left(-\frac{2ig}{\hbar\omega^2}\right) \left(\sin[\omega t/2]^2\right) \\
&+ \left(-\frac{iv_r}{\hbar\omega}\right) \left(\sin[\omega t] - \sin[\omega|t|] - 2\sin[\omega(t-T)] + 2\sin[\omega|t-T|] + \sin[\omega(t-2T)] - \sin[\omega|t-2T|]\right) \\
&+ \left(\frac{iv_z}{2\hbar\omega}\right) \left(\sin[\omega t] + \sin[\omega|t|]\right) + \left(\frac{8v_r}{\hbar\beta}\right) \left(\cos[\omega t] \cos[\omega T] \sin[\omega T/2]^2\right) + \left(\frac{8v_r\beta}{\hbar\omega^2}\right) \left(\sin[\omega t] \sin[\omega T] \sin[\omega T/2]^2\right) \\
G_2[t] &= \left(\frac{2ig}{\hbar\omega^2}\right) \left(\sin[\omega t/2]^2\right) \\
&+ \left(-\frac{iv_r}{\hbar\omega}\right) \left(\sin[\omega t] - \sin[\omega|t|] - 2\sin[\omega(t-T)] + 2\sin[\omega|t-T|] + \sin[\omega(t-2T)] - \sin[\omega|t-2T|]\right) \\
&+ \left(-\frac{iv_z}{2\hbar\omega}\right) \left(\sin[\omega t] + \sin[\omega|t|]\right) + \left(-\frac{8v_r}{\hbar\beta}\right) \left(\cos[\omega t] \cos[\omega T] \sin[\omega T/2]^2\right) + \left(-\frac{8v_r\beta}{\hbar\omega^2}\right) \left(\sin[\omega t] \sin[\omega T] \sin[\omega T/2]^2\right)
\end{aligned}$$

For both sequences, in the limit $\omega \rightarrow 0$, the edge values can be expressed in terms of the unperturbed classical trajectory, as written in Eq. 11.

$$\begin{aligned}
G_1[t] &= \frac{i}{\hbar} x_{\text{cl},1}^{(0)}[t] \\
G_2[t] &= -\frac{i}{\hbar} x_{\text{cl},2}^{(0)}[t]
\end{aligned}$$

where $x_{\text{cl},1}^{(0)}[t]$ is the unperturbed classical trajectory of one interferometer arm, and $x_{\text{cl},2}^{(0)}[t]$ is the unperturbed classical trajectory of the other interferometer arm.

Appendix B: Calculating Diagram Vertex Values

Here we will validate the expression for the vertex value (Eq. 8) by mirroring a method by which vertex values can be computed in QFT. We will take Taylor expansions and functional derivatives to manually compute the value of a tree level 1-vertex diagram, then extract the value associated with the vertex of that diagram. Consider Eq. 1, rewritten here as

$$\langle 0|0\rangle_J = e^{i \int d^4x \epsilon \mathcal{L}_1 \left[\frac{1}{i} \frac{\delta}{\delta J[x]}\right]} Z_0[J] \quad (\text{B1})$$

with

$$Z_0[J] = e^{\frac{i}{2} \int d^4x_1 \int d^4x_2 J[x_1] G[x_1, x_2] J[x_2]}$$

One way to determine the value of a vertex for the diagrams which compose the solution to $\langle 0|0\rangle_J$ is to Taylor expand Z_0 and the functional in Eq. B1, then apply functional derivatives to compose a first order tree level diagram manually.

Consider the interaction term $\mathcal{L}_1 = \frac{\epsilon n}{n!} \varphi^n$. It happens that the tree level diagram that is first order in ϵ will emerge from the 1st order Taylor series coefficient of the functional in Eq. B1, and the n^{th} order Taylor series coefficients of $Z_0[J]$. These two terms can be written as

$$\left(\int d^4x \frac{i\epsilon c_n}{n!} \left(\frac{1}{i} \frac{\delta}{\delta J[x]} \right)^n \right) \left(\frac{1}{n!} \left(\frac{i}{2} \int d^4x_1 \int d^4x_2 J[x_1] G[x_1, x_2] J[x_2] \right)^n \right)$$

Using the identities $\frac{\delta}{\delta J[x]} J[x_1] = \delta[x - x_1]$ and $G[x_1, x_2] = G[x_2, x_1]$, the result of applying one functional derivative to the functional can be written as

$$\left(\int d^4x \frac{\epsilon c_n}{i^{n-1} n!} \left(\frac{\delta}{\delta J[x]} \right)^{n-1} \right) \underbrace{\left(\frac{i^n}{2^n n!} \left(\int d^4x_1 \int d^4x_2 J[x_1] G[x_1, x_2] J[x_2] \right)^{n-1} \right)}_{\text{factor 1}} \underbrace{\left(\int d^4x_3 J[x_3] G[x_3, x] \right)^1}_{\text{factor 2}}$$

where the factor of $2n$ comes from the $2n$ J functions that are acted on by $\delta/\delta J[x]$. Now consider applying another functional derivative to 'factor 1' (applying it to 'factor 2' would result in a loop in the diagram, and we are aiming to construct just the tree level diagram). This results in

$$\left(\int d^4x \frac{\epsilon c_n}{i^{n-1}n!} \left(\frac{\delta}{\delta J[x]} \right)^{n-2} \right) \underbrace{\left(\frac{i^n}{2^n n!} \left(\int d^4x_1 \int d^4x_2 J[x_1] G[x_1, x_2] J[x_2] \right)^{n-2} \right)}_{\text{factor 1}} 2^{2n(n-1)} \underbrace{\left(\int d^4x_3 J[x_3] G[x_3, x] \right)^2}_{\text{factor 2}}$$

Then if we keep applying functional derivatives 'factor 1' until we are out of functional derivatives, we will be left with

$$\left(\int d^4x \frac{\epsilon c_n}{i^{n-1}n!} \right) \left(\frac{i^n}{2^n n!} 2^n n! \left(\int d^4x_3 J[x_3] G[x_3, x] \right)^n \right) = \frac{1}{n!} \frac{\epsilon c_n}{i^{n-1}} \int d^4x (iG[x])^n$$

where $G[x] = \int d^4x' J[x'] G[x', x]$. Since this one-vertex tree level diagram is going to have symmetry factor $1/n!$ And we define the value of all the external edges which contribute to the diagram to be $(iG[x])^n$. We have therefore determined that the value of the vertex is equal to $\frac{\epsilon c_n}{i^{n-1}} \int d^4x$, as written in Sec. II A.

Now we apply the same analysis to the diagrams which compose phase shifts in matter wave interferometry. We consider the expression of Eq. 6, re-written here as

$$C e^{i\Delta\phi} = \exp \left[\int_{t_i}^{t_f} dt_1 \epsilon \left(\underbrace{\frac{i}{\hbar} \delta_{a1} L_1 \left[\frac{\hbar}{i} \frac{\delta}{\delta J_a[t_1]} \right]}_{\text{term 1}} + \underbrace{\frac{-i}{\hbar} \delta_{a2} L_1 \left[\frac{\hbar}{-i} \frac{\delta}{\delta J_a[t_1]} \right]}_{\text{term 2}} \right) \right] Z_0[J] \quad (\text{B2})$$

with

$$Z_0[J] = e^{\frac{1}{2} \int_{t_i}^{t_f} dt_1 \int_{t_i}^{t_f} dt_2 J_b[t_1] G_{bc}[t_1, t_2] J_c[t_2]}$$

We first consider applying the functional derivatives of 'term 1'. Consider an L_1 of the form $L_1 = \frac{c_n}{n!} z^n$, the contribution to the tree level one-vertex diagram will come from the first order expansion of the functional in Eq. B2, and the n^{th} order expansion of $Z_0[J]$:

$$\left(\epsilon \int_{t_i}^{t_f} dt \frac{i}{\hbar} \delta_{a1} \frac{c_n}{n!} \left(\frac{\hbar}{i} \frac{\delta}{\delta J_a[t]} \right)^n \right) \left(\frac{1}{n!} \left(\frac{1}{2} \int_{t_i}^{t_f} dt_1 \int_{t_i}^{t_f} dt_2 J_b[t_1] G_{bc}[t_1, t_2] J_c[t_2] \right)^n \right)$$

Now using the identities $\frac{\delta}{\delta J_a[t]} J_b[t_1] = \delta_{ab} \delta[t - t_1]$ and $G_{ab}[t_1, t_2] = G_{ba}[t_2, t_1]$, the result of applying one functional derivative from the left hand side to the functional on the right hand side can be expressed as

$$\left(\int_{t_i}^{t_f} dt \frac{\epsilon c_n}{n!} \left(\frac{\hbar}{i} \right)^{n-1} \delta_{a1} \left(\frac{\delta}{\delta J_a[t]} \right)^{n-1} \right) \times \left(\frac{1}{n! 2^n} \underbrace{\left(\int_{t_i}^{t_f} dt_1 \int_{t_i}^{t_f} dt_2 J_b[t_1] G_{bc}[t_1, t_2] J_c[t_2] \right)^{n-1}}_{\text{factor 1}} \delta_{ae} 2n \underbrace{\left(\int_{t_i}^{t_f} dt_3 J_d[t_3] G_{de}[t_3, t] \right)^1}_{\text{factor 2}} \right)$$

where the factor of $2n$ emerges in the same way it did in the QFT case. After applying all functional derivatives to 'factor 1' as before, we arrive at

$$\left(\int_{t_i}^{t_f} dt \frac{\epsilon c_n}{n!} \left(\frac{\hbar}{i} \right)^{n-1} \delta_{a1} \right) \left(\frac{1}{n! 2^n} \delta_{ae} 2^n n! \left(\int_{t_i}^{t_f} dt_3 J_d[t_3] G_{de}[t_3, t] \right)^n \right) = \frac{1}{n!} \epsilon c_n \left(\frac{\hbar}{i} \right)^{n-1} \delta_{a1} \int_{t_i}^{t_f} dt G_a[t]^n$$

where $G_a[t] = \int_{t_i}^{t_f} dt' J_{a'} G_{a'a}[t', t]$. The symmetry factor of the diagram is $1/n!$ And the value of all the external edges are $G_a[t]^n$, so the vertex value is given by $\epsilon c_n \left(\frac{\hbar}{i} \right)^{n-1} \delta_{a1} \int_{t_i}^{t_f} dt$. Doing the same analysis with 'term 2' in Eq. B2

results in a vertex value of $\epsilon c_n \left(\frac{\hbar}{-i}\right)^{n-1} \delta_{a2} \int_{t_i}^{t_f} dt$. It happens that even beyond the first order expansion in ϵ , these two separate vertex values can be combined into a single vertex whose value is a sum of the two. The rest of this section will illustrate this concept. Let us first consider these two terms ('term 1' and 'term 2') in Eq. B2 to contribute two distinct vertices. We can draw the vertex associated with 'term 1' with a filled-in circle, and the vertex associated with 'term 2' as a hollow circle:

$$\begin{array}{c} \left. \begin{array}{c} \text{---} \\ \text{---} \\ \text{---} \\ \vdots \\ \text{---} \end{array} \right\} n \text{ edges} \\ \bullet \\ t, a \end{array} = \eta_{a1}^n \int_{t_i}^{t_f} dt \qquad \begin{array}{c} \left. \begin{array}{c} \text{---} \\ \text{---} \\ \text{---} \\ \vdots \\ \text{---} \end{array} \right\} n \text{ edges} \\ \circ \\ t, a \end{array} = \eta_{a2}^n \int_{t_i}^{t_f} dt$$

where

$$\eta_{jk}^n = \epsilon c_n \left(\frac{\hbar}{i(-1)^{k+1}}\right)^{n-1} \delta_{jk}$$

Consider a diagram with m vertices indexed by $i = 1, 2, \dots, m$, where vertex i is an n_i -point vertex. Such a diagram will emerge from taking the following functional derivatives of $Z_0[J]$ in Eq. B2.

$$\begin{aligned} & \prod_{i=1}^m \frac{1}{n_i!} \int_{t_i}^{t_f} dt_i \left(\eta_{a_i1}^{n_i} \left(\frac{\delta}{\delta J_{a_i}[t_i]}\right)^{n_i} + \eta_{a_i2}^{n_i} \left(\frac{\delta}{\delta J_{a_i}[t_i]}\right)^{n_i} \right) \\ &= \frac{1}{\prod_{i=1}^m n_i!} \left(\int_{t_1}^{t_f} dt_1 \int_{t_2}^{t_f} dt_2 \dots \int_{t_m}^{t_f} dt_m \right) \sum_{b_1, b_2, \dots, b_m \in \{1, 2\}} \prod_{i=1}^m \eta_{a_i b_i}^{n_i} \left(\frac{\delta}{\delta J_{a_i}[t_i]}\right)^{n_i} \end{aligned}$$

where the sum is over all the 2^m combinations of b_1, b_2, \dots, b_m , with each taking the values of 1 or 2, and vertex i is labeled ' t_i, a_i ' for $i = 1, 2, \dots, m$. The sum comes from expanding out all the terms in the product over i in the left hand side. Consider a diagram that comes out of one of the elements in this sum, corresponding to one possible set of values for b_1, b_2, \dots, b_m . We can express the value of this diagram as

$$\left(\prod_{i=1}^m \eta_{a_i b_i}^{n_i} \right) \mathcal{E}[a_1, a_2, \dots, a_m]$$

where included in the function \mathcal{E} are the edge values, the symmetry factor of the diagram, and the integrals over time associated with the vertices. The sum over the possible values of b_1, b_2, \dots, b_m can be written as

$$\sum_{b_1, b_2, \dots, b_m \in \{1, 2\}} \left(\prod_{i=1}^m \eta_{a_i b_i}^{n_i} \right) \mathcal{E}[a_1, a_2, \dots, a_m] = \left(\prod_{i=1}^m (\eta_{a_i1}^{n_i} + \eta_{a_i2}^{n_i}) \right) \mathcal{E}[a_1, a_2, \dots, a_m] = \left(\prod_{i=1}^m \lambda_{a_i}^{n_i} \right) \mathcal{E}[a_1, a_2, \dots, a_m]$$

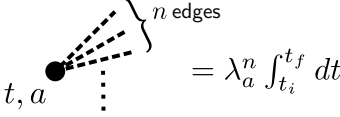
where $\lambda_a^n = \eta_{a1}^n + \eta_{a2}^n$, so that the value of each of the m vertices can be expressed as a sum of the corresponding hollow or filled-in n_i -point vertices. As an example, consider a perturbative potential $L_1 = \frac{c_3}{3!} z^3 + \frac{c_4}{4!} z^4$, and a diagram which contributes to the phase shift at first order in c_3 and second order in c_4 under this potential. In this case, $m = 3$, and we label vertices so that $n_1 = 3, n_2 = n_3 = 4$. For notational convenience, we write $a_1 = a, a_2 = b, a_3 = c$. The 2^3 different possible values of b_1, b_2 , and b_3 will produce 8 diagrams, whose sum can be written as

$$\begin{array}{c} \begin{array}{cccccccc} \begin{array}{c} \text{---} \\ \text{---} \\ \bullet \\ t_1, a \\ \text{---} \\ \text{---} \\ \bullet \\ t_2, b \\ \text{---} \\ \text{---} \\ \bullet \\ t_3, c \end{array} & + & \begin{array}{c} \text{---} \\ \text{---} \\ \circ \\ t_1, a \\ \text{---} \\ \text{---} \\ \bullet \\ t_2, b \\ \text{---} \\ \text{---} \\ \bullet \\ t_3, c \end{array} & + & \begin{array}{c} \text{---} \\ \text{---} \\ \bullet \\ t_1, a \\ \text{---} \\ \text{---} \\ \circ \\ t_2, b \\ \text{---} \\ \text{---} \\ \bullet \\ t_3, c \end{array} & + & \begin{array}{c} \text{---} \\ \text{---} \\ \bullet \\ t_1, a \\ \text{---} \\ \text{---} \\ \bullet \\ t_2, b \\ \text{---} \\ \text{---} \\ \circ \\ t_3, c \end{array} & + & \begin{array}{c} \text{---} \\ \text{---} \\ \circ \\ t_1, a \\ \text{---} \\ \text{---} \\ \circ \\ t_2, b \\ \text{---} \\ \text{---} \\ \bullet \\ t_3, c \end{array} & + & \begin{array}{c} \text{---} \\ \text{---} \\ \circ \\ t_1, a \\ \text{---} \\ \text{---} \\ \bullet \\ t_2, b \\ \text{---} \\ \text{---} \\ \circ \\ t_3, c \end{array} & + & \begin{array}{c} \text{---} \\ \text{---} \\ \bullet \\ t_1, a \\ \text{---} \\ \text{---} \\ \circ \\ t_2, b \\ \text{---} \\ \text{---} \\ \circ \\ t_3, c \end{array} & + & \begin{array}{c} \text{---} \\ \text{---} \\ \circ \\ t_1, a \\ \text{---} \\ \text{---} \\ \circ \\ t_2, b \\ \text{---} \\ \text{---} \\ \circ \\ t_3, c \end{array} \end{array} \\ & (\eta_{a1}^3 \eta_{b1}^4 \eta_{c1}^4 + \eta_{a2}^3 \eta_{b1}^4 \eta_{c1}^4 + \eta_{a1}^3 \eta_{b2}^4 \eta_{c1}^4 + \eta_{a1}^3 \eta_{b1}^4 \eta_{c2}^4 + \eta_{a2}^3 \eta_{b2}^4 \eta_{c1}^4 + \eta_{a2}^3 \eta_{b1}^4 \eta_{c2}^4 + \eta_{a1}^3 \eta_{b2}^4 \eta_{c2}^4 + \eta_{a2}^3 \eta_{b2}^4 \eta_{c2}^4) \mathcal{E}[a, b, c] \\ &= (\eta_{a1}^3 + \eta_{a2}^3)(\eta_{b1}^4 + \eta_{b2}^4)(\eta_{c1}^4 + \eta_{c2}^4) \mathcal{E}[a, b, c] \\ &= \lambda_a^3 \lambda_b^4 \lambda_c^4 \mathcal{E}[a, b, c] \end{array}$$

with

$$\mathcal{E}[a, b, c] = \frac{1}{4} \int_{t_i}^{t_f} dt_1 \int_{t_i}^{t_f} dt_2 \int_{t_i}^{t_f} dt_3 (G_a[t_1]G_b[t_2]G_c[t_3]G_{bc}[t_2, t_3]^2 G_{ba}[t_2, t_1]G_{ca}[t_3, t_1])$$

where the factor of 1/4 comes from the symmetry factor of the diagram. The two terms in Eq. B2 (referred to as 'term 1' and 'term 2'), can therefore be associated with a single vertex, rather than two distinct ones. The vertex value associated with the perturbative term $L_1 = \frac{c_n}{n!} z^n$ can be written as



The diagram shows a central black dot representing a vertex. From this dot, several dashed lines radiate outwards, representing edges. A curly brace on the right side of these lines is labeled "n edges". Below the vertex, the text "t, a" is written. To the right of the diagram, the mathematical expression $= \lambda_a^n \int_{t_i}^{t_f} dt$ is shown.

where

$$\lambda_a^n = \epsilon c_n \left(\left(\frac{\hbar}{i} \right)^{n-1} \delta_{a1} + \left(\frac{\hbar}{-i} \right)^{n-1} \delta_{a2} \right)$$

as is expressed in Eq. 8.

